Thalamic state controls timing and synchronization of primary somatosensory cortical representations in the awake mouse

Peter Y Borden[1*], Nathaniel C Wright[1*], Arthur E Morrissette[2], Dieter Jaeger[2], Bilal Haider[1], Garrett B Stanley[1]

[1] Wallace H Coulter Department of Biomedical Engineering, Georgia Institute of Technology and Emory University, Atlanta, GA, USA

[2] Emory University, Department of Biology, Atlanta, Georgia, USA

*Denotes co-first authorship

Abbreviated Title: Thalamic state controls timing and synchronization of S1 cortex

With 41 text pages, 8 Figures

Correspondence: Garrett B Stanley
Coulter Department of Biomedical Engineering
Georgia Institute of Technology & Emory University
313 Ferst Drive
Atlanta GA 30332-0535
USA

Phone: 404-385-5037
Fax: 404-385-5044
Email: garrett.stanley@bme.gatech.edu

Conflict of Interest: The authors declare no competing financial interests.

Acknowledgements: This work was supported by NIH National Institute of Neurological Disorders and Stroke Grant R01-NS048285 (GBS), R01-NS104928 (GBS), U01-NS094302 (GBS and DJ), and NIH National Institute of Neurological Disorders and Stroke Pre-doctoral NRSA NS098691 (PYB).

Summary (150 words max, currently 150)

The thalamus controls transmission of sensory signals from periphery to cortex, ultimately shaping perception. Despite this significant role, dynamic thalamic gating and the consequences for downstream cortical sensory representations have not been well studied in the awake brain. We optogenetically modulated the ventro-posterior medial thalamus in the vibrissa pathway of the awake mouse, and measured spiking activity in the thalamus, and at the level of primary somatosensory cortex (S1) using extracellular electrophysiology and genetically encoded voltage imaging. Thalamic hyperpolarization significantly amplified thalamic sensory-evoked spiking through enhanced bursting, yet surprisingly the S1 cortical response was not amplified, but instead timing precision was significantly increased, spatial activation more focused, and there was an increased synchronization of cortical inhibitory neurons. A thalamocortical network model implicates the precise timing of feedforward thalamic spiking, and timing-sensitive engagement of synaptic depression, presenting a highly sensitive, state-dependent timing-based gating of sensory signaling to cortex.

INTRODUCTION

We explore the world through our sensory periphery, where sensors transduce the signals that ultimately give us perception of the world. The mammalian sensory thalamus gates information from the periphery to primary sensory cortices, controlling what signals do and do not make their way to cortex, thus playing a very critical role in sensing. Far from a static relay, the thalamus is under continuous influence by modulatory inputs from brainstem and feedback mechanisms from cortex (Sherman and Guillery, 2002; Sherman, 2005), most extensively explored in the context of sleep and epileptic seizures (Huguenard and McCormick, 2007; Fogerson and Huguenard, 2016). The large majority of detailed thalamic studies focusing on its potential role in sensory signaling have been either in ex-vivo/slice preparations or in intact/in-vivo preparations under anesthesia, where prominent thalamic properties such as synchronization of convergent thalamocortical projections and tonic/burst gating have been shown to strongly boost signaling under these conditions (Murray Sherman, 2001; Sherman, 2001; Swadlow and Gusev, 2001; Swadlow, 2002; Lesica and Stanley, 2004; Lesica et al., 2006; Wang et al., 2010; Stanley et al., 2012; Whitmire et al., 2016, 2021). Recent studies exploring the role of thalamus in the awake, unanesthetized brain have confirmed the critical role of thalamus in grossly modulating sensory cortex (Halassa et al., 2011; Poulet et al., 2012a; Lewis et al., 2015; Reinhold et al., 2015; Yu et al., 2016). However, whether increases in thalamic excitability act to boost cortical sensory-evoked responses in the awake brain as predicted from ex-vivo and anesthetized studies is unknown.

In addition to direct afferent inputs that serve as the primary drive of thalamocortical activity, thalamic nuclei receive more subtle modulatory inputs from a range of sources, including corticothalamic feedback (McCormick and von Krosigk, 1992; Crandall et al., 2015a), thalamic reticular nucleus (Halassa and Acsády, 2016), as well as diffuse inputs from the reticular formation (Castro-Alamancos, 2002) and reticular activating system (Rodenkirch et al., 2019) and other neuromodulatory centers (for a review, see Varela, 2014). The coordinated and collective effects of this complex array of excitatory and inhibitory inputs sets the operating point, or *state*, for thalamic neurons, which can vary widely in different conditions. These modulations in baseline thalamic excitability have important implications for both spontaneous and sensory-evoked thalamic firing activity, which interact to ultimately shape thalamic drive of cortex. Even small changes in baseline membrane potential have been shown to have appreciable effects on spontaneous firing of thalamic neurons (Béhuret et al., 2015), setting the overall tone of synaptic drive to cortex. The use of pharmacology to directly modulate thalamic state (Godwin et al., 1996; Hirata and Castro-Alamancos, 2010; Poulet et al., 2012b) or opto/microstimulation and pharmacology to indirectly affect thalamic state through cortical (Olsen et al., 2012; Mease et al., 2014; Crandall et al., 2015b; Li and Ebner, 2016; Kirchgessner et al., 2020) and subcortical (Aguilar and Castro-Alamancos, 2005) inputs has further causally

revealed the sensitivity of cortex to overall thalamic drive. Importantly, thalamic neurons also exhibit distinct tonic versus burst firing modes (Sherman, 2001), the switching of which is highly sensitive to baseline membrane potential, and the de-inactivation of T-type calcium channels (Suzuki and Rogawski, 1989; Kim et al., 2015). Neurons in the thalamus contain T-type calcium channels that are normally inactivated, but become activated through prolonged hyperpolarization. Subsequent depolarizing inputs lead to "bursts" of action potentials. Most actively investigated in the context of sleep states and rhythmic discharge, the role of this mechanism in sensory signaling remains unclear. Because thalamocortical high frequency bursting events have been shown to have a significant impact on downstream cortical activation (Swadlow and Gusev, 2001), the state-dependent gating of thalamic signaling through the aggregate effects of all these properties is hypothesized to serve a critical role in processing sensory information (Crick, 1984; Sherman and Guillery, 2002; Sherman, 2005); however, this has not been investigated extensively in the intact brain due to the lack of methodological approaches to precisely manipulate thalamic state properties. To date, no studies have utilized temporally precise, repeatable and reversible modulation to precisely measure the effects of thalamic state and burst/tonic gating in awake cortex at the level of population signals and single neuron firing.

Here, we directly determined how thalamic gating properties control sensory-evoked thalamic and cortical responses in the vibrissa pathway of the awake, head-fixed mouse. Instead of driving or silencing neural activity, optogenetic manipulation was used to modulate thalamic state while recording extracellular thalamic and cortical activity and acquiring widefield cortical voltage imaging, using the voltage indicator ArcLight (Jin et al., 2012; Borden et al., 2017). We found that baseline thalamic firing rate was surprisingly invariant to optogenetic thalamic hyperpolarization through a transition from tonic to burst firing activity, and the baseline activity in S1 cortex was correspondingly invariant to thalamic hyperpolarization, following a brief transient increase in firing activity. In response to sensory stimuli, the thalamic hyperpolarization significantly amplified the thalamic evoked response through enhanced bursting; however, the magnitude of the response in S1 cortex was not amplified, but instead slightly attenuated relative to baseline, despite the amplification in thalamic drive. However, the sensory evoked response was also significantly more brief and spatially focused, and accompanied by an increase in the synchronization of the putative cortical Fast-spiking (FS) inhibitory neurons. A thalamocortical network model replicated these findings, and implicated the precise timing of feedforward thalamic spiking, and the corresponding timing-sensitive engagement of thalamocortical synaptic depression, as a likely mechanism underlying the experimental observations. Taken together, the results here point to timing rather than response magnitude as a fundamental feature of the thalamocortical circuit, presenting a dynamic, state-dependent timing-based gating of sensory signaling to cortex.

METHODS

All procedures were approved by the Institutional Animal Care and Use Committee at the Georgia Institute of Technology and were in agreement with guidelines established by the National Institutes of Health.

AAV Delivery: At least 5 weeks prior to experimentation, 6 week old female C57BL/6J (Jackson Laboratories) mice were injected with different viral constructs either in the ventral posteromedial (VPm) thalamic region with AAV-5-CamKinaseII-eNph3.0 (UNC Viral Vector core) for optogenetic modulation, in the primary somatosensory (S1) cortex with AAV-1-hsyn1-ArcLight (UPenn Viral Vector Core) for optical voltage imaging, or both. For surgical procedures, mice were anesthetized using isoflurane (3-5%). After the mouse was fully anesthetized, small craniotomies were placed over the regions of interest and were aligned using stereotaxic measurements (For VPm, 1.8mm lateral from midline by 1.8mm caudal from bregma). For cortical expression, either single or multiple injection sites were used surrounding the barrel cortex (centered at 1.5mm caudal from bregma and 3mm lateral from midline). The virus was loaded into a modified Hamilton syringe (701-N) with a ~35 micron borosilicate glass pipette tip or a Hamilton Neuros Syringe. The syringe was initially lowered to the corresponding depth below the surface (for VPm: 3mm and For S1: 0.5mm) and the tissue was allowed to rest for 1 minute before injection. Both sites received injections of 0.5-1μl of viral construct at a flow rate of 0.1μl/minute. After injection, the pipette remained in place for an additional 5 minutes before slowly being removed from the brain. The bore holes were filled with either bone wax or left to close naturally. Throughout injection, mice were kept warm using a water heating system to maintain body temperature. See Supplemental Figure S1 for histological validation of expression of halorhodopsin in thalamus and ArcLight in S1.

Awake Animal Preparation: At least four weeks after ArcLight and eNphR3.0 viral injection, mice were anesthetized under isoflurane and were implanted with a head-plate. Over the course of 5-14 days preceding the first imaging experiment, mice were routinely handled to gain familiarity with the imaging system and immobilization device. During this acclimatization period, mice were head fixed for increasingly longer periods of time, from 15 minutes to 1.5 hours. During stimulation of the whisker, mice were prevented from interacting with the whisker stimulator by obstructing the path from the paws to the whisker. Mice were rewarded with sweetened milk (Nestle, Ltd.) throughout imaging. After at least 5 days of handling and acclimating, mice became tolerant to immobilization in the headplate restraint system. During passive stimulation of the whiskers, the mice often actively moved their whiskers. Therefore, the whisker stimulator was placed relatively close (5mm) to the face to prevent the whisker from slipping out of the manipulator;

however, the amplitude of the deflection was adjusted to maintain a consistent angular velocity (1200 deg/s).

Whisker Stimulation: Whisker stimulation was similar to that utilized previously (Borden et al., 2017). Briefly, individual vibrissae of the mice were deflected by a high fidelity (1 KHz) galvanometer system (Cambridge Technologies). A whisker stimulus was applied by positioning the custom designed galvanometer 5-10mm from the face and delivering an exponential sawtooth (rise and fall time = 5ms). The waveform stimulus velocity was taken by averaging the time to peak velocity of the stimulus. The velocity was adjusted based on distance from the face.

Thalamic and Cortical Electrophysiology: For thalamic electrophysiology, a small craniotomy was made over the primary whisker sensitive thalamic ventral-posterior medial (VPm) region of the mouse, around the injection site (see above). First, the VPm was mapped with a 2MOhm tungsten electrode (FHC) which was slowly lowered until 2.5mm below the cortical surface. The mouse VPm was identified using both stereotaxic measurements and depth as well as electrophysiological features (such as latency, peak response, whisker selectivity). A neuron was determined to be located in the VPm if the peri-stimulus time histogram (PSTH) contained a peak response 3ms -10ms after a 1200 degree/s (deg/s) punctate single whisker stimulation and did not have a latency shift by more than 20ms after 1s of a 10Hz adapting stimulus (Wang et al., 2010). The principal whisker was first determined using a manual probe to isolate the whisker with the largest evoked response. If further isolation was needed, the principal whisker was determined by the largest 30ms PSTH response of the surrounding three whiskers. Note that VPm single units were difficult to isolate in the awake animal, limiting our sample size, but the multi-unit VPm activity is also reflective of the same findings. For cortical recordings, initial mapping was conducted using cortical ArcLight voltage imaging or intrinsic imaging (see below). Once the target cortical column (barrel) was identified and confirmed, a 32-channel silicon probe (NeuroNexus) or single tungsten electrode was inserted. For both thalamic and cortical electrophysiology, after the conclusion of the study either a small 7uA 10s lesion, or a fluorescent dye was placed near the recording location and confirmed using post-mortem histological validation. Neuronal signals were band-pass filtered (500Hz–5KHz), digitized at 30 KHz/channel and collected using a 96-channel data-acquisition system (Blackrock Microsystems, Salt Lake City, UT, USA). For single unit recordings, offline spike sorting was accomplished using Plexon Offline Spike Sorter v4 (Plexon, Inc). For multi-unit data, we measured threshold crossings from the continuously recorded thalamic or cortical activity. Thalamic multiunit activity was captured using a threshold criterion of 5 standard deviations over the entire recording (Yang et al., 2016). For cortical multiunit recordings, a manual threshold was set based on each experiment. Additional data analysis utilized custom scripts using Matlab (Mathworks, Inc).

Awake Cortical Fluorescent ArcLight Imaging: ArcLight transfected mice were imaged through the thinned or removed skull using a two camera system: a Scimedia Imaging system to measure cortical ArcLight spatial activity, and a custom camera to measure hemodynamic activity for subtraction. The cortex was imaged using a 184 x123 pixel CCD Camera, MiCam2 HR Camera (Scimedia, Ltd) to capture ArcLight, and a Basler Ace (acA1920-155um) 480 x 180 pixel (4x4 binned) CMOS Camera to capture auto-fluorescence, at 200 Hz with a tandem lens microscope. The entire cortical area was illuminated at 465 nm with a 400 mW/cm2 LED system (Scimedia, Ltd.) to excite the ArcLight fluorophore and background auto-fluorescence. The excitation light was projected onto the cortical surface using the first dichroic mirror (bandpass: 475/625nm, Semrock, Inc.). Collected light was passed through a second dichroic mirror (Longpass cutoff: 495 nm, Semrock, Inc.) for collection of the ArcLight and auto-fluorescence signal. The auto-fluorescence signal was filtered with a bandpass filter between the wavelengths of 465/75 nm (Semrock, Inc). The ArcLight signal was filtered with a bandpass emission filter between wavelengths of 520⁄35 nm (Semrock, Inc.). The imaging system was focused approximately 300µm below the surface of the brain or cortical layer 2/3.

Anesthetized Cortical Fluorescent ArcLight & Intrinsic Imaging: ArcLight transfected mice were imaged through the thinned or removed skull using a Scimedia Imaging system to measure cortical spatiotemporal activity (leveraging a single camera setup). The cortex was imaged using a 184x123 pixel CCD Camera, MiCam2 HR Camera (Scimedia, Ltd) at 200 Hz, and a tandem lens macroscope. The entire cortical area was illuminated at 465 nm with a 400 mW/cm^2 LED system (Scimedia, Ltd.) to excite the ArcLight fluorophore. The excitation light was further filtered (cutoff: 472-430 nm bandpass filter, Semrock, Inc.) and projected onto the cortical surface using a dichroic mirror (cutoff: 495 nm, Semrock, Inc.). Collected light was filtered with a bandpass emission filter between wavelengths of 520-535 nm (Semrock, Inc.). The imaging system was focused approximately 300µm below the surface of the brain to target cortical layer 2/3. For intrinsic imaging of the hemodynamic response, the cortical surface was illuminated by a 625nm red LED (ThorLabs), and imaged with the same camera system as above, at a temporal resolution of 10Hz. During intrinsic imaging, no emission filters were used. In order to evoke a cortical intrinsic response, the whisker was repetitively stimulated at 10Hz for 6 seconds.

Functional Fluorescent Mapping of Barrel Cortex: The mouse's whisker system was first mapped by imaging the rapid ArcLight response to a high velocity (1200 Deg/s) sensory stimulus separately applied to three different whiskers. The resulting whisker response averaged over 20 trials was determined to be associated with a principal whisker, and barrel, if the evoked response was spatially limited to roughly a 0.2 mm x 0.2 mm area 25-30ms after stimulation. Additionally, the response was determined to be originating

from the barrel field if the center of mass of activation moved consistently with the histologically defined barrel field and was within the standard stereotaxic location of S1 (~3mm lateral, 0.5-1.5mm from bregma). After mapping, a single whisker was deflected in a way as to emulate a high velocity slip-stick event (1200 deg/s), either with or without thalamic optogenetic hyperpolarization.

Simultaneous Imaging and Thalamic Optogenetic Manipulation: After mapping both the thalamic and cortical regions, an optrode (2M Ohm tungsten electrode mounted to an 200um optic fiber) was positioned to the stereotaxic locations of the pre-mapped thalamic region and lowered to the corresponding depth. Once a single thalamic unit was identified using the above constraints, the unit was determined to be sensitive to optical stimulation by briefly (1-2s) hyperpolarizing the cells using ~17mW/mm^2 (LED condition) or ~35mW/mm^2 (double LED condition) (unless otherwise noted) at 590nm from an LED light source (Thorlabs, M590-F1). Each cell was determined to be a thalamic optically sensitive unit if the lighted caused a transient decrease in firing rate or if the cessation of the 590nm light caused a rebound burst (Brecht and Sakmann, 2002). After identifying an optically sensitive thalamic unit, the whisker stimulus was presented under various light conditions. Light stimulation was presented 500-750ms preceding and following whisker deflection. There was at least a four second interval between stimulus deliveries to allow for recovery of halorhodopsin (eNphR3.0). Each session imaged 200ms-1s of frames preceding whisker stimulation to measure spontaneous activity. Prior to use, light power was measured from the tip of the ground optical fiber before each experiment to maintain approximate light intensities delivered to each cell. During light delivery, the downstream cortical response was recorded using either electrodes for cortical electrophysiology or voltage imaging as described above. The optogenetic and viral expression of each experiment was verified through confocal and brightfield imaging of fixed slices.

The LED light intensity used for optogenetic stimulation is within the published range of light stimulation (35mW/mm^2 is estimated from our maximum power measure of 1.2mW through a 200um fiber) (Stujenske et al., 2015; Owen et al., 2019). Further, studies that have directly quantified the effects of optical stimulation on local tissue heating and neural activation (in the absence of opsin expression) have found no significant difference in the firing rate change for 1mW light intensity (Stujenske et al., 2015) or minor firing rate changes for 3mW light intensity, but no behavioral effects (Owen et al., 2019). See Supplemental Figure S5 for controls that demonstrate a lack of light effects and lack of confounding interactions between optogenetic activation of VPm thalamus and GEVI imaging in cortical S1.

Anesthetized Electrophysiology: A subset of experiments was conducted with mice under light anesthesia, as a control. These mice were initially anesthetized using isoflurane (3-

5%) and then placed on a heated platform (FHC, Inc.) in a stereotaxic nose cone to maintain anesthesia. A large incision was placed over the animal's skull, and the connective tissue and muscle surrounding the skull was removed using a fine scalpel blade. A modified headplate was attached using dental acrylic (Metabond) and secured to the skull. For cortical imaging, the skull was thinned with a dental drill until transparent, or removed entirely and covered with saline or ringers solution. After surgery, the isoflurane levels were dropped to ~<1% for imaging and electrophysiology, the procedures for which were identical to those for the awake animal. The animal's vitals (heart rate and respiratory rate) were constantly measured for tracking anesthesia depth.

Histology: Histological procedures were similar to those utilized previously (Borden et al., 2017), to validate ArcLight in S1 and/or opsin expression in VPm thalamus. Histological samples were prepared by perfusing the animal transcardially with phosphate buffered saline (PBS) followed by 4% paraformaldehyde. Brains were post-fixed overnight in 4% paraformaldehyde then transferred to PBS before sectioning. Thick sections were cut using a vibratome (100 μm, Leica, VTS 1000) and either directly mounted or saved for staining. See Supplemental Figure S1 for histological validation of expression of halorhodopsin in VPm and ArcLight expression in cortex.

Thalamic Electrophysiology Data Analysis - Mean Response and Burst Ratio: We report several different basic measurements of spiking activity from our thalamic units including evoked response and evoked bursting response. Thalamic firing activity was reported as PSTHs with units of firing rate in Hz, calculated as the number of spikes within a bin, divided by the size of the bin (see individual plots for bin size). We determined thalamic evoked response as the initial response (0-30ms) to sensory stimuli, reported as the number of spikes per stimulus averaged over many trials (9-102 trials). The corresponding evoked bursting response was determined as number of bursting spikes per trial in that same post stimulus period. Bursting spikes were defined as 2 or more spikes that fire at most 4ms apart preceded by 100ms of silence. The 100ms pre-stimulus activity is based on reported values for T-type calcium bursts (Swadlow and Gusev, 2001; Whitmire et al., 2016). All data analysis of the recorded extracellular thalamic units was accomplished using custom Matlab scripts.

Cortical Electrophysiology Data Analysis: Putative single cortical units were identified offline using open-source spike sorting software (KiloSort2). In order to be considered well isolated, each neural unit must have signal to noise ratio greater than 2, and have less than 1% of spikes within 0-1ms Inter-spike Interval (ISI). Although recordings originated across cortical layers, for simplicity, all units were analyzed in the same pool, regardless of the laminar origin. Individual single-units were classified as putative Regular Spiking Units (RSUs) or Fast Spiking Units (FSUs) based on the characteristics of the spike waveform (McCormick et al., 1985; Niell and Stryker, 2010; Guo et al., 2017;

335 Speed et al., 2019; Yu et al., 2019). Specifically, units with a spike-width exceeding 0.4
336 ms (defined as trough-to-peak) were classified as RSUs, and below this as FSUs. Cortical
337 firing activity was reported as PSTHs with units of firing rate in Hz, calculated as the
338 number of spikes within a bin, divided by the size of the bin (see individual plots for bin
339 size). All spikes within a 1ms ISI were removed from analysis. Synchrony across cortical
340 single-units was computed from spike cross-correlograms across recorded pairs.
341 Specifically, synchrony was defined as proportion of spikes from the full (+/- 100ms)
342 cross-correlogram that were in a central +/- 7.5ms window (Wang et al., 2010; Whitmire
343 et al., 2016). To determine the number of needed synchronous events to accurately
344 measure synchrony, we simulated two neurons with a ~5% change in synchrony
345 (assuming a normal distribution). We found that approximately 50 events were required
346 to accurately separate the two distributions.
347
348 Voltage Imaging Data Processing: Raw images were loaded and converted from the
349 SciMedia ". gsd" format using custom scripts and down-sampled by a factor of two. Each
350 dataset was first normalized to a $\%\Delta F/F_o$ measurement by subtracting and dividing each
351 trial by the temporal average of the frames 0 to 200ms preceding light delivery (F_o). In
352 two instances, where 200ms of preceding LED onset activity was not captured, the Fo
353 was taken as an average 200ms period across no-stimulus trials. Hemodynamic noise
354 was removed using a PCA background subtraction method. As described in detail
355 (Borden et al., 2017), *in vivo* ArcLight imaging overlaps with the hemoglobin absorption
356 spectrum, and therefore contains hemodynamic noise that must be removed for analysis.
357 Imaging the wildtype mouse cortical surface using the same blue excitation and ArcLight
358 filter set revealed similar patterns of oscillatory activity, likely through auto-fluorescence
359 and effects of hemodynamic absorption and blood flow (Ma et al., 2016). The background
360 PCA subtraction utilizes the auto-fluorescence signal from non-ArcLight transfected
361 regions to predict the hemodynamic signal across the recorded space. Specifically, the
362 method uses principal component analysis of non-expressing low background auto-
363 fluorescence regions (determined from the maximum fluorescence from a non-injected
364 animal) to find the ongoing hemodynamic components on a single trial basis. Additionally,
365 the background fluorescence regions were selected at least 1mm away from the recorded
366 whisker evoked response (Borden at el, 2017). Ideally, these criteria would create a
367 spatially defined region with little or no ArcLight fluorescence to isolate the hemodynamic
368 signal from the signal of interest. Each frame is first spatially averaged by either a 200
369 µm x 200 µm circular averaging (pillbox) filter or a media filter to reduce noise. On a single
370 trial, the corresponding top five principal components of the low background regions
371 (which contains approximately 85% of the variance explained) are projected on a pixel by
372 pixel basis across the entire recording using a lasso regression method with
373 regularization. The lasso regression utilizes a cross-validated approach to determine the
374 minimum number of components to develop the model of hemodynamic noise. In order

375 to prevent the removal of any stimulus evoked activity, each pixel was fit on pre-stimulus
376 activity (either before light onset for experiments involving optogenetics, or immediately
377 preceding stimulus delivery). The final predicted hemodynamic signal for each pixel was
378 subtracted across the entire recording on a pixel by pixel basis. Due to the complex
379 waveform of the hemodynamic response, a simple notch filter is not effective at
380 separating the signal from the noise (Borden et al., 2017). We found that the background
381 PCA subtraction method greatly reduced hemodynamic signal across the entire frame,
382 compared to the off-ROI method (Borden et al, 2017). In some instances, brief onset and
383 offset light artifacts of the 590nm light was visible in the recorded ArcLight cortical signal.
384 To account for any optogenetic transient light artifacts, we only considered the relative
385 changes in fluorescence during steady state light levels. Both raw and processed images
386 showed qualitatively similar results.
387
388 Awake Voltage Imaging Data Analysis –Dual Camera: In the awake animal, we utilized a
389 dual camera imaging system to capture a background fluorescence signal for
390 hemodynamic subtraction. Two different cameras were used to capture the ArcLight and
391 auto-fluorescence signals, and therefore, pixels could not be directly registered for
392 subtraction for pixel by pixel correction. Instead, we utilized the same Background PCA
393 subtraction method to find and develop models of the hemodynamic response based on
394 the global PCA signal derived from the background image. For the dual camera data,
395 each component was fit over the entire recording for subtraction of the hemodynamic
396 noise. Both raw and processed images showed qualitatively similar results. Unless
397 otherwise noted, each dataset was processed with the Background PCA or Dual Camera
398 subtraction method as stated above.
399
400 Imaging Data Analysis – Peak amplitude, Normalized Peak, and Temporal Properties:
401 We measured the effect of the optogenetic stimulation on the peak amplitude of the
402 evoked mean ArcLight fluorescence in the determined cortical barrel. The cortical barrel
403 region of interest (ROI) for each stimulated barrel and each data set was selected as the
404 200 μm x 200 μm region with the largest response 30ms after stimulus delivery. This
405 determined ROI was used for all subsequent analyses of the temporal response. To better
406 isolate the evoked amplitude, the frame preceding stimulus delivery (t=-5ms) was
407 subtracted from the resulting recorded signal. For each recording, the peak amplitude
408 was defined as the $\Delta F/F_o$ at the time of the maximum average response between 0 and
409 110ms for the strongest stimuli (1200 Deg/s) presented under control and various
410 optogenetic conditions. In order to measure the temporal properties of the evoked
411 response, we concentrated on the timeseries data from the determined cortical barrel
412 ROI. For normalized fluorescence (Norm ΔF/Fo), each session's peak response was
413 divided by the average peak response to the strongest stimulus (1200 Deg/s) under the
414 control condition. The normalization allows for a better comparison across animals which
415 may have different levels of ArcLight expression. Peak time was defined as the time of

the maximum fluorescence between 0 and 110 ms post stimulus, and the time of return to baseline as the time when the fluorescence crossed the pre-stimulus baseline value following the peak. Peak-to-baseline was then calculated as the time between the fluorescence peak and the return of the fluorescence to baseline. Recovery was defined as the average fluorescence in the 120-400ms window following the stimulus.

Imaging Data Analysis – Area Measurements: In addition to measuring the peak response, we also measured the effect of different thalamic states on the evoked area of sensory cortical activity. We measured the activated area as the number of pixels exceeding a threshold using the average response at the peak frame (0-110ms) preceding stimulus delivery. Similar to other studies (Lustig et al., 2013; Millard et al., 2015), we measured the spatial activation using the 70% threshold. To compare the area independent of amplitude changes, we normalized the peak frame by dividing by the peak fluorescence in each condition (Control and LED). In order to isolate the evoked activity from ongoing activity, we subtracted the frame preceding stimulus delivery (t=-5ms). Different thresholds had no effect on the observed trends.

Whisking Recordings and Analysis: In all analyses, we included electrophysiological and voltage imaging data regardless of the behavioral state of the animal, which invariably combines data during whisking and non-whisking periods. As a control, we measured the awake whisking behavior using a Basler Ace (acA1920-155um) camera sampled with 480 x 300 pixel (4x4 binned) at 20-50 Hz. The whiskers were illuminated using either an external LED light (860nm) or by the imaging 465nm light source. Images were continually recorded through the entire recorded session and then aligned using the movement of the galvo stimulus. A select region of interest (ROI) was placed in the whisker pad close to the face to determine changes in average intensity during the recording session. A custom algorithm measured the squared change in intensity to determine periods of whisker movement. Whisker movement was assigned using a threshold of pixel intensity that was used for each imaging session. A movements had to last longer than 100ms to considered as whisking periods. Any trial with a whisking periods within 500ms of the stimulus were determined to be a whisking trial. As shown in Supplemental Figure S4, analyses performed on data parsed based on whisking confirm that the observed trends were consistent across whisking and non-whisking periods.

Integrate & Fire or Burst (IFB) Modeling: The Integrate and Fire or Burst (IFB) model was derived from previously published models of thalamic function from the LGN (Smith et al., 2000; Lesica and Stanley, 2004; Lesica et al., 2006) and VPm (Whitmire et al., 2016). In order to simulate the experimental parameters and account for changes in thalamic activity, some additional terms and parameters were added and adjusted. Additionally, we generated ongoing activity using two methods, either injected current noise or synaptic

events, with both showing the same results. The results shown here use the synaptic event model where IPSCs and EPSCs are modulated as fixed inputs. The model itself was written and analyzed using custom scripts in Matlab 2016a.

The model is based on modifications of the standard integrate and fire model representing the effects of integrated synaptic currents on membrane voltage:

$$C\frac{dV}{dt} = I_{EPSC} - I_{IPSC} - I_L - I_T - I_{Halo}$$

$$I_L = g_L(V - V_L),\ I_T = g_T m_\infty h(V - V_T)$$

$$\frac{dh}{dt} = \begin{cases} \frac{-h}{\tau_h^-}, (V > V_h) \\ \frac{(1-h)}{\tau_h^+}, (V < V_h) \end{cases}$$

$$\frac{dI_{EPSC}}{dt} = \frac{I_{EPSC}}{\tau_s}$$

$$\frac{dI_{IPSC}}{dt} = \frac{I_{IPSC}}{\tau_s}$$

The following parameters were used to simulate thalamic activity: $C = 2\mathrm{uF}/cm^2$, $g_L = 0.035\ \mathrm{mS}/cm^2$, $g_T = 0.07\ \mathrm{mS}/cm^2$, $\mathrm{V}_L = -65\mathrm{mV}$, $\mathrm{V}_{reset} = -45\mathrm{mV}$, $\mathrm{V}_h = -68\mathrm{mV}$, $\mathrm{V}_T = 120\mathrm{mV}$, $\tau_h^+ = 0.1\mathrm{s}$, $\tau_h^- = 0.02\mathrm{s}$, $\tau_s = 1\mathrm{e} - 2\mathrm{uF}/cm^2$, $Threshold = -35\mathrm{mV}$, $I_{Halo} = 0 - 1uA/cm^2$. EPSPs occurred at a rate $\mathrm{EPSP}_{rate} = 1 - 25\mathrm{Hz}$, where each excitatory post-synaptic event had a peak of $3\mathrm{nA}/cm^2$, and decayed according to the above first-order differential equation for I_{EPSC}. Similarly, IPSPs occurred at a rate of $\mathrm{IPSP}_{rate} = 0 - 5\mathrm{Hz}$, where each inhibitory post-synaptic event had a peak of $1uA/cm^2$, and decayed according to the above first-order differential equation for I_{IPSC}. To simulate the different levels of thalamic activity, we varied the rates of EPSP inputs on the thalamic model (based on published ranges of thalamic activity (Urbain et al., 2015)). IPSPs were simulated at a much lower rate (20% of EPSP rate) to add additional variability to baseline activity. The model outputs represent the average response of a 100 simulated thalamic neurons in response to various levels of thalamic hyperpolarization and baseline activity. The model was updated at 1ms steps. The absolute refractory period was set to 1ms.

<u>Cortical E-I Modeling:</u> We constructed a simple model of the thalamocortical network using custom scripts written in Python 3.6.10, as described previously (Wright et al., 2021) We modeled a single cortical barrel as a clustered network of excitatory and inhibitory single-compartment leaky integrate-and-fire (LIF) neurons, subject to excitatory thalamic and non-thalamic synaptic inputs. For both the “Control” and “LED” conditions, we simulated 50 trials, each lasting 200 ms, with a time-step of 0.05 ms. A detailed

492 description of the model can be found in Cortical E-I Modeling Supplemental, Section 1.
493 All code is freely available upon request.
494
495 Non-zero thalamocortical (TC) synaptic weights were broadly distributed, and we
496 implemented differential TC connectivity by imposing higher TC convergence (Bruno and
497 Simons, 2002; Cruikshank et al., 2007) and shorter synaptic latencies (Cruikshank et al.,
498 2007a; Kimura et al., 2010a) for inhibitory neurons, and requiring that VPm neurons with
499 the highest rates synapsed only onto inhibitory neurons (Bruno and Simons, 2002).
500
501 We modeled a single cortical column as a network of 800 excitatory and 100 inhibitory
502 LIF neurons, with relatively strong inhibitory-to-excitatory synapses (Gabernet et al.,
503 2005). We imposed spatial clustering via "small-world" network connectivity (Litwin-
504 Kumar and Doiron, 2012; Bujan et al., 2015; Wright et al., 2017a, 2017b), with 10% re-
505 wiring probability. Inhibitory LIF neurons had shorter membrane time constants (Gentet
506 et al., 2010) and refractory periods than excitatory neurons, which – together with the TC
507 connection properties described above – supported higher firing rates in inhibitory
508 neurons, as observed here (Fig. 6B, C) and in previous work (Bruno and Simons, 2002;
509 Khatri et al., 2004; Gentet et al., 2010; Taub et al., 2013). Excitatory neurons were subject
510 to an inhibitory spike-rate adaptation conductance, which helped to stabilize network
511 activity.
512
513 We drew tonic and burst thalamic spike times from the empirical VPm spike time PSTHs,
514 with bursts modeled as either pairs (in the Control condition) or triplets (in the LED
515 condition) of spikes with 2.5 ms ISI. In response to a spike in a given thalamic neuron,
516 all TC synapses from that neuron decayed instantly and recovered slowly.
517
518 We employed four alternate models to parse the roles played by TC synaptic adaptation,
519 changes in thalamic firing (i.e., burst ratio and the overall time-course of evoked firing),
520 and intracortical inhibition. For each model, we calculated the grand mean +/- SEM firing
521 rates for all neurons, for a 50 ms pre-stimulus window, and an "early" (0 – 50 ms post-
522 stimulus) and "late" (60 – 100 ms post-stimulus) response window, where stimulus onset
523 time represents the time of galvo deflection onset, or $t = 0$ in the empirical VPm PSTH.
524 For synchrony analysis, we randomly selected 200 excitatory and 200 inhibitory neuron
525 pairs.
526
527 <u>Statistical Analysis & Data Sharing:</u> All tests were conducted using the MATLAB Statistics
528 Toolbox (Mathworks, Inc.). For all measurements, we determined if the specific data sets
529 were normally distributed using the Lilliefors test for normality. If the data were normal,
530 we used the appropriate (paired or unpaired) t-test for statistical difference. If the
531 population was determined to have non-normal distributions, we conducted non-

parametric Wilcoxon signed-rank tests to determine statistical significance. All sample sizes are reported in the figure captions and Results text, along with an indication of particular test and the corresponding statistical significance level (* - $p<0.05$, ** - $p<0.01$, *** - $p<0.001$ in figures). All datasets and software are available upon request.

RESULTS

All experiments were conducted in the vibrissa pathway of the mouse (Figure 1A). To directly test the predictions of previous in-vitro and anesthetized work, we conducted the first experiment in the isoflurane-anesthetized mouse (illustrated in Figure 1B). In the lightly anesthetized mouse, we utilized extracellular electrodes to record whisker-evoked spiking activity in VPm thalamus, in the presence (LED, ~17mW/mm^2, 590nm) and absence (Control) of a hyperpolarizing optogenetic modulation of excitatory thalamic relay neurons expressing halorhodopsin (eNphR3.0, see Supplemental Figure S1), through a small fiber optic cable attached to the electrode (Figure 1B). Note that the inhibitory opsin was engaged with a constant illumination at a range of relatively low light levels, to induce sustained hyperpolarization, as opposed to complete inactivation. Note also that the total amount of light delivered here was in a range that has been previously shown to not induce significant heating of the surrounding tissue (see Methods), and control experiments indicate that there is no effect of the light alone in the absence of opsin expression (Supplemental Figure S5). Although the in-vivo optogenetic implementation precludes precise knowledge of the degree of hyperpolarization of the thalamic neurons due to variations in opsin expression, position of optic fiber relative to cells, etc., a separate set of in-vitro, slice experiments showed that VPm neurons were hyperpolarized by ~15-25 mV for the light levels utilized (see Supplemental Figure S2). Given that in the in-vitro experiments, light was presented more directly to the VPm neurons expressing halorhodopsin, and that in the in-vivo experiments the presentation of light did not completely silence the neurons, it is likely that the in-vitro experiments were an upper-bound for the in-vivo case, and the actual hyperpolarization induced in-vivo was less than that of the in-vitro experiments.

Neurons in VPm thalamus responded to a single, computer-controlled punctate whisker stimulation (1200 deg/sec, sawtooth waveform) with a brief, transient sequence of action potentials (Figure 1D, see Methods for single unit and multi-unit classification). The sensory evoked thalamic VPm response was significantly amplified by optogenetic thalamic hyperpolarization, as shown in Figure 1D (all spikes in black, putative T-type calcium “burst” spiking in red, classified according to the criterion in Figure 1C). Shown in the insets are the low baseline firing rates in the anesthetized condition. Overall, there was a ~35% increase in the evoked response from the Control to the LED condition

572 (Figure 1E left, black, p=0.0046, paired Wilcoxon signed-rank, n=29 units), in large part
573 driven by the increase in sensory evoked thalamic bursting (Figure 1E left, red, p=4.5e-
574 4, paired Wilcoxon signed-rank, n=29 units). In a subset of experiments, we recorded the
575 downstream cortical multiunit activity (Figure 1E right), and found a corresponding
576 increase during the period of hyperpolarization (n=102 trials, 2 recordings, 1 mouse).
577 Additionally, we simultaneously recorded cortical S1 activation at a meso-scopic scale
578 with optical voltage imaging in primary somatosensory (barrel) cortex using a Genetically
579 Engineered Voltage Indicator (GEVI, ArcLight, Borden et al., 2017) during optogenetic
580 hyperpolarization of thalamus (see Methods). This approach enables the characterization
581 of the overall spatiotemporal changes in S1 due to the thalamic manipulation
582 (Supplemental Figure S5). The imaging was focused at a cortical depth consistent with
583 layer 2/3, where it captured sub-threshold activity reflective of suprathreshold layer 4 input
584 to layer 2/3 (Petersen et al., 2003). The fluorescence imaging of cortical S1 confirmed a
585 corresponding amplification of the sensory evoked response during thalamic
586 hyperpolarization (raw %dF/Fo), as shown in an example session for the fluorescence
587 images in Figure 1F and further quantified across the larger dataset in the left panel of
588 Figure 1G (normalized relative peak evoked response, ~60% increase, 1G inset raw
589 relative peak evoked %dF/Fo, p=0.017, paired Wilcoxon signed-rank, n=13 recordings
590 across 9 mice). There was an amplification in the peak response, followed by a relatively
591 fast transient decrease in fluorescence, followed by a gradual return to baseline over
592 approximately 200ms. The results here using optogenetic manipulation of thalamus and
593 wide-field voltage imaging of cortex are consistent with previous observations of
594 spontaneous thalamic bursting and the impact on downstream synaptic targets in cortical
595 layer 4 (Swadlow and Gusev, 2001). Importantly, the amplification in the peak response
596 observed here under these conditions reflects what would have been expected from the
597 observations in thalamus, if the cortical sensory representation were solely shaped by the
598 amplitude of the feedforward thalamic inputs.
599

600 **Thalamic State and Ongoing Thalamic and Cortical activity in the awake brain**

601 In a next set of experiments, we sought to characterize the influence of thalamic state
602 properties on gating of signaling to cortex in the awake mouse. Before turning to the
603 sensory-evoked responses, we first probed the effect thalamic hyperpolarization has on
604 baseline, ongoing activity that is significantly higher in the awake state as compared to
605 under anesthesia. The baseline firing rate in the awake state is significantly higher than
606 in the anesthetized condition, and we thus expect to see some effect of the optogenetic
607 hyperpolarization on baseline firing. An example single-unit VPm recording (experimental
608 setup in Figure 2A) is shown in the raster plot in Figure 2B. VPm neurons in awake mice
609 exhibited moderate ongoing firing activity (4.9 Hz for this example). Upon presentation of
610 a ramping optical input to thalamus (LED, 590nm, ~17mW/mm^2), the spiking activity
611 underwent a qualitative change to a more sparse pattern of multiple action potentials,

typical across all recorded cells. Bursts were present in the baseline (Control, no light) condition, but substantially more prevalent in the presence of the hyperpolarizing optogenetic input. This effect is summarized across all clearly identified single-units in the top panel of Figure 2C (n=5), showing the average instantaneous firing rate for all spiking in black, and for the putative burst spiking in red (bands represent +/- 1 standard error of the mean, SEM). This shows that following an initial decrease in firing rate at the onset of the light ramp, the VPm firing activity returned to the same overall pre-stimulus baseline firing rate. This was accompanied by a monotonic increase in the burst firing rate, suggesting that the return to pre-stimulus baseline firing rate was due to a compensatory transition from tonic to burst firing. Note that the VPm nucleus in mice is a very small structure, difficult to target and difficult to identify and maintain clearly isolated single units in the awake state, thus we conservatively classified several of the recordings as multi-unit in nature, which precludes burst/tonic identification. This same net effect we observed in the single units is also shown in the bottom panel of Figure 2C for the multi-unit data (n=9 recordings). The multi-unit firing rate did not significantly change from the Control (0 mW/mm^2) to the hyperpolarized condition (Figure 2D left, multi-unit, Control vs LED p= 0.098, Control vs Double LED p= 0.65, Wilcoxon signed-rank, n=9 MU recordings; ~17mW/mm^2 - LED or ~35mW/mm^2 - Double LED). Note that the firing rate in the LED conditions was calculated from the 250-750ms window, after the initial transient decrease in firing rate. This lack of sustained effect on the overall thalamic firing rate was also evident in the single-units (Figure 2D, middle, in the Control condition (n= 8 units) as compared to the activation of the halorhodopsin (n= 5 units), for both all spikes (black) and spikes classified as belonging to a burst (red). While there was no significant change in the overall single-unit firing rate (black, Control vs LED p=0.55, Control vs Double LED p= 0.37, unpaired t-test), there was a significant increase in the firing rate associated with bursting (red, Control vs LED p=0.014, Control vs Double LED p= 0.032, unpaired t-test), indicating a compensatory shift from tonic to burst firing with the thalamic hyperpolarization resulted in a significant increase in the burst ratio metric from the Control to hyperpolarized condition (Fig. 2D, right, Control vs LED p=0.0016, Control vs Double LED p=0.0016, unpaired Wilcoxon rank sum test). Further examination showed that increasing hyperpolarization also increased the number of spikes per burst (illustrated in left of Figure 2E), which partially offsets the loss of tonic spiking (right of Figure 2E, Control vs LED p=0.048, Control vs Double LED p= 0.016, unpaired Wilcoxon rank sum test, n=5 units across conditions, only considered units that had bursts).

Although it is not surprising that the thalamic burst mechanism was engaged by the optogenetic hyperpolarization, it is surprising that the net baseline firing rate was not decreased, but was instead invariant to the thalamic hyperpolarization. This effect was not as apparent in the anesthetized condition when the baseline thalamic firing rate is near zero, but emerges in the awake state where baseline thalamic firing rate is

652 significantly higher. To investigate possible causes, we constructed an integrate-and-fire
653 or burst (IFB) model of thalamic firing that has been utilized in previous studies (Smith et
654 al., 2000; Lesica and Stanley, 2004; Lesica et al., 2006), where the resting membrane
655 potential was set by the level of activation of the hyperpolarizing opsin (see Methods).
656 When the model neuron was set to have a spontaneous, baseline firing rate consistent
657 with our observations (~5 Hz), the effect of the hyperpolarizing opsin activation indeed
658 replicated this phenomenon (Figure 2F). An initial decrease in firing rate at the onset of
659 the light ramp was followed by a return to pre-light baseline level of firing (compare with
660 Figure 2C). Moreover, as in the experimental observation, the return to the baseline firing
661 rate in the hyperpolarized condition is dominated by the increase in bursting activity in the
662 IFB model (Figure 2F, red). The exact combination of the baseline activity and intensity
663 of the hyperpolarizing input strongly influenced the net resultant effect (Supplemental
664 Figure S3). Prolonged periods of halorhodopsin activation have been shown to potentially
665 alter the reversal potential of chloride (Raimondo et al., 2012). However, due to the short
666 timescales of LED stimulation used in this work (1-1.5s), and the large transition to burst
667 firing, the effect shown here is more likely driven by low voltage activation of T-type
668 calcium channels, further reinforced by the IFB model.
669
670 To uncover the downstream effects of the above observations in VPm, we performed the
671 same optogenetic manipulations during multi-electrode recording of single-unit activity in
672 S1 in the awake mouse (Figure 3A). Shown in the top panel of Figure 3B is a raster plot
673 from one example session (10 trials each from 15 simultaneously recorded units), in
674 response to the optogenetic hyperpolarization of thalamus with the LED (again 590nm,
675 17mW/mm^2). This example demonstrates a clear transient increase in spiking with the
676 thalamic hyperpolarization, typical of the cortical recordings. The bottom panel of Figure
677 3B shows the aggregate single-unit firing rate, with a clear transient increase in firing rate
678 at the light onset (bands represent +/- 1 SEM), with a gradual return to the baseline, pre-
679 hyperpolarization level of firing rate at steady-state. Figure 3C summarizes this trend,
680 showing the mean single-unit firing rate across recorded cortical single-units in the
681 Control condition (0mW/mm^2) versus activation of halorhodopsin in thalamus (LED -
682 17mW/mm^2 or Double LED - 35mW/mm^2), for the initial increase in firing rate during a
683 transient period (300-350 ms, open symbols) and the subsequent return to baseline firing
684 rate at steady state (700-750 ms, closed symbols). There was a significant transient
685 increase in the cortical firing rate across both led conditions (transient, Control vs LED
686 p=5.4e-14, Control vs Double LED p= 1.4e-15, Wilcoxon signed-rank test, n=118 units).
687 After the transient increase, we observed a subsequent return to near baseline, either
688 with no net effect or a marginal increase in the rate (steady-state, Control vs LED p=0.2,
689 Control vs Double LED p= 0.013, Wilcoxon signed-rank test). Interestingly, following
690 thalamic hyperpolarization, the cortical firing rate appeared to begin its initial transient
691 increase while the thalamic activity remained relatively low (Figure 2), which could reflect

692 an increased sensitivity of the thalamocortical synapse following the initial period of
693 quiescence (Swadlow and Gusev, 2001; Swadlow et al., 2005)
694
695 Taken together, the results here suggest that in response to the optogenetically induced
696 thalamic hyperpolarization, the thalamic VPm neurons in the awake mouse exhibit a
697 transient decrease in baseline firing rate, followed by a return to approximately pre-
698 hyperpolarization level that is at least partially explained by a trade-off between tonic and
699 burst firing, while the downstream activity in cortical S1 exhibits a transient increase in
700 baseline firing rate, followed by an eventual return to approximately the original baseline
701 rates.
702
703 **Thalamic State and Sensory Evoked Thalamic and Cortical Activity**
704 We next recorded the sensory evoked single-unit activity in VPm thalamus in the
705 presence and absence of thalamic hyperpolarization in the awake mouse (Fig. 4A).
706 Neurons in VPm thalamus responded to a single, computer-controlled punctate whisker
707 stimulation (1200 deg/sec, sawtooth waveform) with a brief, transient increase in multi-
708 unit activity (see Methods), which was significantly boosted with thalamic
709 hyperpolarization (Fig. 4B; PSTH across multi-units, LED approximately 17mW/mm^2, n=9
710 recordings, 2 mice). Overall, there was an approximately 85% increase in the sensory
711 evoked response of the thalamic MU VPm neurons with optogenetic hyperpolarization
712 (Figure 4C, Control vs LED p=0.0039, Control vs Double LED p=0.0039, paired Wilcoxon
713 signed-rank, n=9 recordings, 2 mice). To explore the potential role of tonic/burst gating in
714 the boosting of the thalamic response, we analyzed clearly identified VPm single-units
715 where spiking could be classified as tonic or burst in origin. The single-units also exhibited
716 a brief, transient sequence of action potentials (Fig. 4D; PSTH across single-units, n=8
717 for Control, n=5 for LED approximately 17mW/mm^2), qualitatively similar to the multi-unit
718 data and to single-units observed in the anesthetized case. The top plot shows the peri-
719 stimulus time histogram (PSTH, 2 ms bins) for all spikes (black) and putative burst spikes
720 (red). In response to the transient sensory input, in the no-light (Control) condition, there
721 is a short-latency transient VPm spiking response (black), with a modest level of putative
722 T-type calcium bursting (red). In the presence of the hyperpolarizing light input to
723 thalamus (Figure 4D, bottom, LED), however, there is an obvious increase in the VPm
724 response to the sensory input (black), driven by a dramatic increase in bursting response
725 (red), that is qualitatively similar to that in the anesthetized condition. The latency of the
726 sensory-evoked response also increased, consistent with the T-type calcium channel
727 bursts. We tested a range of LED intensities to determine the impact of various levels of
728 thalamic hyperpolarization on the evoked bursting (Figure 4E; LED approximately
729 17mW/mm^2, and Double LED approximately 35 mW/mm^2, for full range see Supplemental
730 S6). With thalamic hyperpolarization, there was a significant increase in single-unit burst
731 ratio (Figure 4E, Control vs LED p=0.011, Control vs Double LED p=0.019, unpaired

Wilcoxon rank sum, n=5 units in 2 mice for (single & double) LED conditions, n=8 units in 3 mice for Control). Taken together, the multi- and single-unit data reveal a boosting of the sensory evoked thalamic response with thalamic hyperpolarization that is likely due to the increased sensory-evoked thalamic bursting.

To examine the downstream consequences of the observed changes in the sensory-evoked response in thalamus, we recorded cortical S1 activation with wide-field optical voltage imaging during optogenetic hyperpolarization of thalamus in the awake mouse (illustrated in Figure 4F, see Methods). Note further that fluorescent imaging approaches like this are differential in nature (responses are based on relative not absolute changes in fluorescence), and are thus not well suited to capture overall absolute levels of ongoing background activity, but instead are targeting evoked responses relative to background. Based on previous findings (Swadlow and Gusev, 2001), the results in the anesthetized mouse, and the amplified sensory-evoked response in thalamus with thalamic hyperpolarization in the awake mouse, we expected to see a corresponding amplification of the cortical sensory-evoked response. Shown in Figure 4F is a trial averaged sequence of the sensory-evoked fluorescence images. Following the deflection at time 0, a localized change in fluorescence began to emerge 10-15 ms later. Surprisingly, thalamic hyperpolarization did not result in an increased cortical response, but instead induced an apparent modest decrease in sensory evoked S1 activity. As quantified in Figure 4G, the peak fluorescence showed an approximately 20-40% decrease with this level of thalamic hyperpolarization (Control vs LED p=0.020, Control vs Double LED p=0.0039, paired Wilcoxon sign rank test, 2 mice over 9 sessions for LED conditions). Note that the right panel of Figure 4G is the same data as in the left panel, with each dataset normalized to the Control condition, to show a percent decrease in the peak fluorescence.

Finally, in a separate set of experiments, we hyperpolarized thalamus while simultaneously recording the S1 Cortical SU responses using a multichannel electrode (illustrated in Figure 4H). The corresponding PSTHs for responses to a punctate whisker stimulus (1200 deg/sec, sawtooth waveform) are shown in Figure 4I (Control (0mW/mm^2) vs. LED (17mW/mm^2) conditions). The average absolute evoked cortical response remained approximately invariant during LED conditions across all cortical recorded units (Figure 4J, left, 5 to 100ms post-stimulus, n=118). However, the evoked cortical spiking relative to baseline decreased with increasing LED intensities (Control vs LED p=0.20, Control vs Double LED p=0.034, paired Wilcoxon signrank, n=118 units, across 3 mice), consistent with the GEVI recordings (Figure 4G), which are relative measures by construction.

To summarize, there is an amplification of the sensory evoked thalamic response with thalamic hyperpolarization, driven by the increase in sensory evoked bursting. Given this

amplification of the thalamic sensory evoked response that serves as the primary feedforward inputs to cortical S1, it was surprising to observe in the awake mouse not an increase, but instead a sensory evoked cortical response that was invariant in absolute amplitude and decreased relative to background activity.

Thalamic State and Spatial and Temporal Sharpening of Sensory Evoked Cortical Response

The GEVI imaging of cortex enables further investigation of the spatial characteristics of the observed phenomenon. Figure 5A shows the imaging frame associated with the peak sensory-evoked fluorescence, for the Control (top) and thalamic hyperpolarization (LED, bottom) conditions. What is apparent qualitatively from the images is that there was an overall attenuation of the cortical evoked response with thalamic hyperpolarization, as previously shown in Figure 4. Less immediately obvious is the effect of the thalamic hyperpolarization on the spatial extent of the sensory evoked cortical activation, as an overall loss in amplitude would trivially produce an apparent loss in spatial activation, as illustrated conceptually in the top panel of Figure 5B – often referred to as the “iceberg” effect. The bottom panel of Figure 5B shows conceptually the alternative - that the reduction in spatial area of activation may not just be due to the reduction in amplitude of the evoked response, but instead can reflect a spatial sharpening of the sensory evoked response with increasing thalamic hyperpolarization after accounting for the decrease in peak amplitude of fluorescence. For the GEVI recordings here, the latter is indeed the case - this is summarized as a reduction in the evoked normalized area of activation in the left panel of Figure 5D (Control vs LED $p=0.025$, Control vs Double LED $p=0.046$, paired t-test, 2 mice over 9 recording sessions for LED conditions).

In addition to the spatial characteristics of the sensory evoked response revealed by the voltage imaging, the voltage imaging is also useful in revealing relatively fast temporal dynamics of the aggregate cortical activity. Figure 5C shows the integrated fluorescence signal within a barrel column in the presence (LED condition) or absence (Control) of light input to activate halorhodopsin in thalamus, giving a picture of the temporal dynamics of the sensory-evoked clear response to the punctate whisker stimulus (2 mice over 9 recording sessions). We again found a decrease of the sensory evoked response (note that the fluorescence in Fig. 5C is normalized) despite a ~85% increase in the sensory-evoked multi-unit response in thalamus as measured in comparable experiments (Fig. 4). Also apparent is the presence of a more rapid, post-peak decay in the fluorescence with thalamic hyperpolarization, and a prolonged period of sub-baseline fluorescence before returning to baseline after several hundred milliseconds. To quantify the temporal sharpening of the sensory evoked response, we calculated the temporal width of the evoked response as the time between the fluorescence peak and the first return to

baseline level (defined as peak-to-baseline, Figure 5C), as shown in the middle panel of Figure 5D, revealing a clear narrowing/sharpening of the temporal response as a function of thalamic hyperpolarization from ~150ms in the Control condition, to ~67ms in the thalamic hyperpolarized condition (Control vs LED p=0.0059, Control vs Double LED p=0.0019, unpaired t-test, LED conditions n=9, Control n=8 recording sessions, note one Control recording did not return to a pre-stimulus baseline). To quantify the prolonged post-stimulus undershoot of activity, we calculated the overall fluorescence in a window from 120 to 400ms post-stimulus (defined as mean recovery in Figure 5C, Control vs LED p=0.016, Control vs Double LED p=0.020, paired t-test, n=9 recording sessions), as shown in the right panel of Figure 5D. The increasingly negative relative fluorescence in this window revealed a clear increase in the undershoot with increasing thalamic hyperpolarization. Taken together, these S1 voltage imaging results show that in addition to the attenuation of the sensory-evoked response with thalamic hyperpolarization, there is a corresponding sharpening of the spatial activation of S1 and a temporal sharpening in the form of a more transient evoked response with an inhibitory undershoot.

Thalamic State and the Cortical Spike Timing

Taken together, the results from Figure 5 revealed that the thalamic hyperpolarization sharpens both the spatial and temporal aspects of the cortical sensory evoked response in the awake brain. The absence of these effects in the anesthetized brain in Figure 1 suggests the potential role of cortical circuitry in shaping the sensory representations, as isoflurane as an anesthetic has been shown to significantly suppress intracortical dynamics (Greenberg et al., 2008; Vizuete et al., 2012; Haider et al., 2013; Aasebø et al., 2017; Suzuki and Larkum, 2020). To further probe this phenomenon, we parsed our cortical single-units into putative excitatory neurons (regular spiking units, RSUs) and putative inhibitory neurons (fast spiking units, FSUs). Specifically, single-unit activity was identified (see Methods) and parsed based on RSU and FSU classification and combined across cortical layers, the result of which is shown in Figure 6A. The top panel shows the waveform for typical putative RSU (red) and FSU (blue), where the solid line represents the mean waveform, and the band represents the standard deviation around the mean. The bottom panel shows the distribution of the time from the trough to the peak for the recorded waveforms. A threshold was set at 0.4 ms based on prior literature ((Guo et al., 2017), see Methods), for classifying the individual units into RSUs or FSUs.

Apparent in the aggregate PSTH is the expected higher baseline/ongoing activity and sensory evoked responses in the FSUs compared to the RSUs, as shown in Figure 6B (~17 HZ for FSU, n=32; ~3 Hz for RSU, n=86), along with several other observations quantified in Figure 6C. As shown in the left panels of Figure 6C, in response to the thalamic hyperpolarization (LED ~17 mW/mm^2, double LED ~35 mW/mm^2), there was a relatively modest increase in baseline (pre-stimulus, -50 – 0 ms) firing rate for RSUs

(Control vs LED p=5.3e-4, Control vs Double LED p=0.012, Wilcoxon signed-rank test, n=86), while FSUs showed no significant change (Control vs LED p=0.15, Control vs Double LED p=0.30, Wilcoxon signed-rank test, n=32). The response to the punctate sensory stimulus was a relatively short latency, transient increase in firing activity in both cell types, appearing to be relatively unchanged in overall magnitude with thalamic hyperpolarization, further quantified in the middle panels of Figures 6C (early response, 5-50ms post stimulus). We observed a slight increase in the RSU evoked firing rate (less than ~10% increase, Control vs LED p=0.067, Control vs Double LED p=0.0082, Wilcoxon signed-rank test, n=86); however, FSUs displayed no statistical difference (Control vs LED p=0.30, Control vs Double LED p=0.45, Wilcoxon signed-rank test, n=32). This same effect was consistent across a larger range of optogenetic light levels (Supplemental Figure S6).

Although the overall magnitude of the early phase of the sensory evoked response was relatively unchanged by the thalamic hyperpolarization for both the FSUs and RSUs, there was a qualitative change in shape of the PSTH, with an increased latency to peak in the early phase, and change in the later phase of the evoked response. Specifically, thalamic hyperpolarization induced a reduction in the later phase of the cortical response, and a dip below the baseline firing rate in both the FSUs and RSUs, as shown in the PSTHs in Figure 6B. This was reflected in a decrease in the late phase (60-100ms) of the evoked response from the Control to the LED condition as shown in the right panels of Figure 6C (RSU - Control vs LED p=0.017, Control vs Double LED p=0.014, n=86, FSU Control vs LED p=2.2e-4, Control vs Double LED p=4.5e-4, n=32, Wilcoxon signed-rank test).

The changes in timing and shape of the PSTHs of the cortical neurons suggest the possibility that thalamic hyperpolarization could affect synchronization within the cortical network. We analyzed synchrony across simultaneously recorded cortical single-units. Synchrony in firing across a pair of Neurons 1 and 2 is evaluated by examining the spike times of Neuron 2 relative to a particular spike of Neuron 1, across all spikes of Neuron 1, as illustrated in Figure 7A (see Methods). This forms the spike cross-correlogram (CCG), from which the synchrony is calculated as the integrated area within a +/- 7.5 ms window (see Methods, (Wang et al., 2010; Whitmire et al., 2016)), as illustrated in the bottom of Figure 7A. Due to the sensitivity of the synchrony metric to firing rate, we only examined pairs with a robust measurement (more than 50 synchronous events) to control for measurement accuracy (experimental results were invariant with different thresholds, see Methods), which restricted the analysis to FSUs in our dataset. Figure 7B shows rasters from an example pair of FSUs in the Control and double LED conditions (top), along with the spikes identified to be synchronous by this criterion (bottom). Figure 7C shows the aggregate cross-correlograms across 99 FSU pairs for the sensory evoked

response, calculated from the spiking in the 100 ms window following the delivery of the sensory stimulus. There is an increase in the concentration of mass around 0 lag with thalamic hyperpolarization, which is indicative of an increased synchrony. This is summarized in Figure 7D, showing a significant increase across FSU units in the measured synchrony (Control vs LED, p=1.5e-8, Control vs Double LED, p=3.5e-13, Wilcoxon signed-rank test, n=99 FSU pairs). For comparison, the synchrony was also computed for the ongoing, spontaneous activity, revealing the synchronizing effect of the transient sensory input. These results were qualitatively similar for various synchrony window sizes (not shown).

Modeling of the thalamic burst driven cortical E-I circuit

We next sought to understand the mechanistic basis of three key experimental results: 1) the invariant absolute S1 sensory response in the thalamic hyperpolarized (LED) condition in the awake mouse, despite the dramatic increase in sensory-evoked (burst) spikes in VPm; 2) the decrease in late (60 – 100 ms post-stimulus) spiking in the S1 response; and 3) the increase in sensory-evoked cortical synchrony in FS neurons in the thalamic hyperpolarized (LED) condition. To explore the potential role of various thalamic and cortical mechanisms, we constructed a simple model of the thalamocortical network, as described previously (Wright et al., 2021). This network mimics the numerical expansion of neurons at the thalamocortical junction, and incorporates several known properties of thalamocortical and intracortical connectivity (Figure 8A, see Methods and Supplemental Information on Cortical E-I Modeling). The network was composed of a single model VPm “barreloid” (40 independent spike trains) projecting to a single barrel “column”, modeled as an interconnected network of 800 excitatory and 100 inhibitory single-compartment leaky integrate-and-fire neurons with clustered connectivity (Litwin-Kumar and Doiron, 2012; Bujan et al., 2015; Wright et al., 2017a, 2017b). For each VPm spike train, ongoing and sensory-evoked VPm tonic and burst spikes were drawn from inhomogeneous Poisson processes matching the empirical tonic and burst VPm PSTHs (Figure 8B, top two rows). Motivated by previous studies of cortical sensory adaptation in brain slice (Gabernet et al., 2005; Cruikshank et al., 2007b, 2010) and in anesthetized (Chung et al., 2002; Gabernet et al., 2005; Heiss et al., 2008; Cohen-Kashi Malina et al., 2013) and awake (Musall et al., 2014) rodents, we modeled rapid sensory adaptation of the thalamocortical (TC) synapse as instantaneous depression and exponential recovery of the TC synapse in response to a thalamic spike (see Methods). For a more detailed description of the model, see Supplemental Information on Cortical E-I Modeling, Section 1.

This model network succeeded in qualitatively reproducing the three results identified above: despite the fact that the VPm evoked rate in a 50 ms post-stimulus window was substantially boosted in the hyperpolarized (LED) condition, there was comparatively little

change in the S1 excitatory and inhibitory early responses (Figure 8B, bottom two rows, and Figure 8C, left). In addition, late cortical spiking in the LED condition decreased significantly compared to the Control condition (Figure 8B, insets in bottom two rows, and Figure 8C, right). Note that unlike the experimental data, synchrony measures from simulated cortical activity were not limited by lack of firing events, enabling synchrony measurements across both sub-populations. We found that the evoked pairwise synchrony of S1 neurons was higher in the LED condition (Fig. 8D – G). In short, the mechanisms incorporated in this model were sufficient to predict the key experimental results. We next sought to identify the minimum set of mechanisms necessary to explain each result (see Supplemental Information on Cortical E-I Modeling, Section 2). To do this, we employed alternate versions of the model described above, and compared simulation results across models to infer the role of each altered parameter.

First, we asked why the early absolute S1 response was invariant to thalamic hyperpolarization, despite the boosted VPm response (Supplemental Information on Cortical E-I Modeling, Section 2.1). We found that the overall increase in evoked VPm rate in the LED condition yielded weaker TC synapses at the time of TC synaptic transmission, due to activity-dependent synaptic depression (Supplemental Figure S7A, B). Further, the short inter-spike intervals within bursts allowed little time between burst spikes for synaptic recovery (Supplemental Figure S7C), and so the high proportion of burst spikes in the LED condition further reduced the mean TC synaptic weight at the time of synaptic transmission relative to the Control condition (Supplemental Figure S7D). When either synaptic adaptation was removed, or the proportion of evoked burst spikes was held fixed, the model S1 early response was instead boosted in the LED condition compared to the Control condition (Supplemental Figure S7E). These results thus demonstrate that the invariance of the early model response was due to more profound TC synaptic adaptation induced by the substantial increase in thalamic bursting in the LED condition. Notably, the S1 response was boosted in the LED condition in the anesthetized condition, and the model also reproduced this result when we additionally assumed that the LED-induced hyperpolarization enhanced sensory-evoked synchrony across VPm units (Fig. S7F, G). Second, we asked why the late S1 response was reduced in the LED condition compared to Control (Supplemental Information on Cortical E-I Modeling, Section 2.2). We found that this reflected the late decrease in VPm firing, as the overall time-course of cortical firing tracked that of VPm (Supplemental Figure S8A, B). Finally, we asked why cortical pairwise synchrony increased in the LED condition (Supplemental Information on Cortical E-I Modeling, Section 2.2). We found that the change in the time-course of VPm firing yielded a higher concentration of cortical spikes at intermediate response latencies, which shaped correlations between pairs of cortical neurons; pairs of cortical spikes were more likely to be separated by short lags, and less

likely to be separated by longer lags, in the LED condition (Supplemental Figure S8C – F).

Taken together, our modeling results demonstrate the sensitivity of cortical sensory representations to thalamic firing. The degree of thalamic bursting and rapid sensory adaptation of TC synapses together determine the efficacy with which VPm spiking drives S1. This predicts the counterintuitive result that enhanced VPm bursting does not result in a boosted S1 response. At longer (tens of milliseconds) timescales, S1 activity levels generally track that of VPm, and the late drop-out of VPm firing in the LED condition is inherited by S1. Finally, the increased S1 synchrony in the LED condition reflects changes in the overall time-course of VPm firing in the 100 ms following sensory stimulus onset.

DISCUSSION

The sensory thalamus controls the flow of signaling from the periphery to cortex, ultimately gating what we do and do not perceive about the outside world. Despite its critical role in sensing, how this circuit controls signaling remains poorly understood. Here, through a range of experimental approaches in the awake, head-fixed mouse, we show that manipulation of thalamic state through hyperpolarization switches the thalamus from a tonic to burst firing mode that serves to amplify thalamic sensory evoked responses. Sensory cortex, on the other hand, exhibits an invariant absolute evoked response despite the increased thalamic input, instead demonstrating increased timing precision, a focusing of spatial activation, and increased synchrony of spiking. Thalamocortical network modeling further reveals that the induced changes in thalamic spike timing and the engagement of thalamocortical synaptic depression by enhanced bursting are sufficient to explain the increase in cortical synchronization and the invariant cortical response amplitude, respectively. The findings here present a highly sensitive, state-dependent timing-based gating of sensory signaling to cortex.

Thalamic Gating and the Effects on Cortex

Given the amplification of sensory evoked thalamic responses in thalamus with thalamic hyperpolarization, the effects on cortex were surprising. The absolute cortical sensory evoked response was invariant to thalamic hyperpolarization in awake mice, despite the boosted thalamic response. Note that the increase in cortical background firing rate and the invariant absolute sensory evoked cortical response amplitude together led to a decrease in the cortical response relative to baseline, which was consistently reflected in both the relative single unit (Figure 4J) and GEVI (Figure 4G) measures. What was enhanced by the thalamic hyperpolarization, however, was instead the timing precision and synchrony of the sensory evoked cortical activity, which are important to understand in terms of the mechanisms underlying this observation and the potential implications for downstream signaling. The modeling results suggest an interplay between the timing related changes in thalamic firing with a shift to burst mode, and the timing dependent depression of thalamocortical synapses, are likely the key role players in the observed dynamics, although more extensive experiments involving causal manipulations of these mechanisms would need to be conducted to more conclusively establish this explanation. Moreover, the enhanced timing and synchrony of the sensory evoked S1 response suggests a potent input for downstream signaling, despite the invariance in firing rate, but corresponding recordings of the S1 recipient regions would be needed to ultimately determine the effect of the changes in S1. Finally, neurons in VPm thalamus sends axonal projections differentially across laminae in S1 (Sermet et al., 2019), likely resulting in variations in the effects of thalamic hyperpolarization on S1 neurons in different cortical layers. Layer specific effects were not targeted in this study, and thus electrode

recordings obtained across laminae were combined. It is likely that the thalamic-timing related effects on S1 activity we report here would be more pronounced in thalamic recipient layers of S1 as compared to layers not receiving direct monosynaptic thalamic input, resulting in a more variable effect in our pooled data. In contrast to the electrode recordings, the optical GEVI imaging approach utilized here captures primarily sub-threshold activity of S1 neurons with cell bodies in layer 2/3 (Petersen et al., 2003), which could explain the more dramatic effects seen in the voltage imaging, although the imaging obscures any differences across excitatory and inhibitory sub-populations.

Invariance in Baseline Thalamic Firing Activity

In this study, we utilized optogenetic hyperpolarization to bias thalamic sensory responses toward bursting, without significantly changing other dynamics that might indirectly impact sensory responses. One particularly surprising finding here was that despite optogenetically induced hyperpolarization of thalamus, the overall baseline firing rate of thalamic neurons was not suppressed, but instead unchanged. Following a transient decrease in firing rate, the recorded VPm neurons returned to their original baseline firing rate. This finding is, however, consistent with other reported observations. In the visual pathway for example, optogenetic excitation of the reticular nucleus (TRN) transiently silences LGN, followed by a return to the original firing rate at steady-state (Reinhold et al., 2015). In the somatosensory pathway, strong photoinhibition attenuated VPm thalamic firing rate, but failed to quench activity altogether (Halassa et al., 2011; Poulet et al., 2012a; Lewis et al., 2015; Reinhold et al., 2015; Yu et al., 2016). The most parsimonious explanation given the observations here is that moderate amounts of hyperpolarization serve to engage the dynamics of the T-type calcium channels that are inactive at normal baseline conditions, effectively compensating for the loss in tonic spiking due to the hyperpolarization. Although the optogenetic approach here does not enable direct observation of the magnitude of the hyperpolarizing input, separate intracellular in-vitro slice experiments where we repeated the protocol while patching on to VPm neurons revealed relatively modest amounts of hyperpolarization that were well-sustained during constant light illumination. This is important, as recent studies have suggested that prolonged activation of specific opsins can have unintended consequences, notably here the possibility of changes in the reversal potential for chloride (Raimondo et al., 2012b), which could theoretically result in changes in the degree of hyperpolarization, although halorhodopsin as a pump is less directly affected by immediate (local) changes in reversal potential as compared to channel-based optogenetics. Further, with halorhodopsin there is the potential for photoinactivation and decreased photocurrents (Zhang et al., 2019), which could also change the degree of hyperpolarization over time. Through the combination of the intracellular control experiments and replication of the primary result through the integrate and fire or burst

(IFB) model, the likelihood that these possible effects played a primary role here is low, especially over the relatively short timescales shown here.

Importantly, beyond the engagement of the T-type calcium channel burst mechanism upon initial hyperpolarization, it would seem that additional hyperpolarization would further push the neuron away from threshold, making it more difficult to burst, which would predict a corresponding decrease in firing rate. However, we found that increased hyperpolarization increased the number of spikes per burst, which served to offset the decrease in the number of bursts with increasing hyperpolarization. The result is a surprisingly resilient mechanism in response to this perturbation. Although other elements of the circuit certainly play a role in this observation (e.g., TRN), the findings here suggest that the intrinsic properties of the thalamic neurons could be a primary mechanism at work.

Thalamic Manipulation and Intrinsic Modulation

The optogenetic manipulation approach here was utilized to gain systematic control over thalamic burst/tonic firing modes to precisely quantify the functional effects at the level of thalamus and primary sensory cortex. This is especially important in the awake, unanesthetized brain, where continuous fluctuations in thalamic state preclude a clear picture of the causal effects of this mechanism in the thalamocortical circuit. It is nevertheless important to place the findings here in the context of naturally occurring fluctuations in thalamic state. Ongoing thalamic spontaneous bursting events were traditionally only associated with slow wave sleep or anesthesia; however, this has been largely disproven, with low rates of bursts occurring both spontaneously and during naturalistic stimuli in awake somatosensory (Swadlow and Gusev, 2001a; Stoelzel et al., 2009; Wright et al., 2021), visual (Niell and Stryker, 2011), and auditory systems (Massaux et al., 2004). The thalamus receives a range of complex, excitatory and inhibitory inputs that interact with the intrinsic cell properties to collectively set the baseline membrane potential and firing rate of these neurons in normal physiological conditions. In the experiments presented here, the mice were awake and head-fixed, but otherwise idling, trained to tolerate the head-fixation with the periodic delivery of a water reward. During the experiments described here, it appeared that the animals remained engaged and were unlikely to spend much time in a state of low arousal, setting the baseline firing rate and level of neuromodulatory input to the thalamus to a corresponding level. Although the optogenetic manipulation here is likely quite strong relative to other modulatory inputs to thalamus, it is true that these other inputs could affect and influence the thalamus in concert with our manipulation. However, any effects from this would likely be averaged out across trials, only contributing to the variability of the measures we present. It is also the case that cortex is under the influence of a range of modulatory inputs, some of which are shared with thalamus, and thus our manipulation of thalamic

state could effectively serve to decouple the two regions, resulting in the thalamus and cortex being in different “states”, a condition which is likely not entirely physiological. However, there is strong evidence that thalamic activity itself is a strong driver of cortical state (Poulet et al., 2012a), and thus the manipulations of thalamic state could indirectly gain control of cortical state as well. To really disentangle these issues of brain state across different structures like the thalamus and cortex, it is likely that approaches such as closed-loop feedback control of neural activity (Bolus et al., 2018, 2021) need to be employed to more strongly and effectively explore the coupling across brain regions.

Potential Role in Sensory Signaling

Almost four decades ago, Crick proposed a provocative hypothesis – that the thalamic-reticular complex serves as a dynamic gate for attentional control of sensory signaling to cortex (Crick, 1984). Further refinement of this idea suggested that the switching between tonic and burst firing modes of thalamic neurons that is facilitated by the unique dynamics of the T-type calcium channels that are prevalent in the thalamus could establish a context dependent signaling (Sherman and Guillery, 2002; Sherman, 2005). In this framework, burst spiking would promote the detection of salient sensory features, while tonic spiking would promote the transmission of details about the nature of the sensory stimulus. Furthermore, the thalamic burst would also potentially provide a “wake-up call” to cortex (Sherman, 2001), garnering attentional resources that ultimately would serve to switch the thalamic mode of firing to tonic through depolarizing corticothalamic feedback. As attractive a framework as this is, it is also a daunting theory to test experimentally due to the complexity of the circuit, the required specificity of recording and manipulation, and ultimately the need to cast in the context of changing states of arousal during trained behaviors. Several studies in the anesthetized brain have shown that thalamic bursting is indeed well driven by the appearance of salient sensory features (Lesica and Stanley, 2004; Alitto et al., 2005; Denning and Reinagel, 2005), that this promotes the detection of change in the sensory input from the perspective of an ideal observer of thalamic spiking (Lesica and Stanley, 2004), and that this sensitivity is strongly shaped by thalamic state (Lesica et al., 2006). Further studies showing the sensitivity of sensory cortex to thalamic bursting (Swadlow and Gusev, 2001) seem to set the stage for at least part of the overarching coding scheme in which case the cortical response would be amplified by the thalamic bursts in “detect” mode, yet none of this has been tested in the awake brain to date. Although the results here in the awake brain demonstrate that the absolute S1 sensory evoked response was invariant to thalamic hyperpolarization and even diminished relative to background cortical activity, despite potent sensory-evoked thalamic bursting, what emerges is increased timing precision, increased focus of spatial activation, and a corresponding synchronization of the cortical sensory-evoked response. Given the likely timing sensitivity of down-stream brain structures in the sensorimotor arc, the synchronization of cortical activity may in fact be a more critical element of cortical

signaling than overall magnitude, supported by recent behavioral work demonstrating the importance of cortical synchrony over firing rate (Jadhav et al., 2009). Taken together, the results here point to timing rather than response magnitude as a fundamental currency of the thalamocortical circuit, presenting a dynamic, state-dependent timing-based gating of sensory signaling to cortex that has strong implications for detectability and discriminability in complex sensory environments.

References

Aasebø IEJ, Lepperød ME, Stavrinou M, Nøkkevangen S, Einevoll G, Hafting T, Fyhn M (2017) Temporal Processing in the Visual Cortex of the Awake and Anesthetized Rat. Eneuro 4:ENEURO.0059-17.2017.

Aguilar JR, Castro-Alamancos M a (2005) Spatiotemporal gating of sensory inputs in thalamus during quiescent and activated states. J Neurosci 25:10990–11002.

Alitto HJ, Weyand TG, Usrey WM (2005) Distinct properties of stimulus-evoked bursts in the lateral geniculate nucleus. J Neurosci 25:514–523.

Béhuret S, Deleuze C, Bal T (2015) Corticothalamic Synaptic Noise as a Mechanism for Selective Attention in Thalamic Neurons. Front Neural Circuits 9:1–21.

Bolus MF, Willats AA, Rozell CJ, Stanley GB (2021) State-space optimal feedback control of optogenetically driven neural activity. J Neural Eng 18:036006.

Bolus MF, Willats AA, Whitmire CJ, Rozell CJ, Stanley GB (2018) Design strategies for dynamic closed-loop optogenetic neurocontrol in vivo. J Neural Eng 15:026011.

Borden PY, Ortiz AD, Waiblinger C, Sederberg AJ, Morrissette AE, Forest CR, Jaeger D, Stanley GB (2017) Genetically expressed voltage sensor ArcLight for imaging large scale cortical activity in the anesthetized and awake mouse. Neurophotonics 4:031212.

Brecht M, Sakmann B (2002) Whisker maps of neuronal subclasses of the rat ventral posterior medial thalamus, identified by whole-cell voltage recording and morphological reconstruction. J Physiol:495–515.

Bruno RM, Simons DJ (2002) Feedforward mechanisms of excitatory and inhibitory cortical receptive fields. J Neurosci 22:10966–10975.

Bujan AF, Aertsen A, Kumar XA, Kumar A, Kumar XA (2015) Role of Input Correlations in Shaping the Variability and Noise Correlations of Evoked Activity in the Neocortex. J Neurosci 35:8611–8625.

Castro-Alamancos MA (2002) Different temporal processing of sensory inputs in the rat thalamus during quiescent and information processing states in vivo. J Neurophysiol 87:946–953.

Chung S, Li X, Nelson SB (2002) Short-term depression at thalamocortical synapses contributes to rapid adaptation of cortical sensory responses in vivo. Neuron 34:437–446.

Cohen-Kashi Malina K, Jubran M, Katz Y, Lampl I (2013) Imbalance between excitation and inhibition in the somatosensory cortex produces postadaptation facilitation. J Neurosci 33:8463–8471.

Crandall SR, Cruikshank SJ, Connors BW (2015a) A Corticothalamic Switch: Controlling the Thalamus with Dynamic Synapses. Neuron 86:768–782.

Crandall SRR, Cruikshank SJJ, Connors BWW, Crandall SRR, Cruikshank SJJ, Connors BWW (2015b) A Corticothalamic Switch: Controlling the Thalamus with Dynamic Synapses. Neuron 86:1–15.

Crick F (1984) Function of the thalamic reticular complex: The searchlight hypothesis. Proc Natl Acad Sci U S A 81:4586–4590.

Cruikshank SJ, Lewis TJ, Connors BW (2007a) Synaptic basis for intense thalamocortical activation of feedforward inhibitory cells in neocortex. Nat Neurosci 10:462–468.

Cruikshank SJ, Lewis TJ, Connors BW (2007b) Synaptic basis for intense thalamocortical activation of feedforward inhibitory cells in neocortex. Nat Neurosci 10:462–468.

1199 Cruikshank SJ, Urabe H, Nurmikko A V., Connors BW (2010) Pathway-Specific Feedforward
1200 Circuits between Thalamus and Neocortex Revealed by Selective Optical Stimulation of
1201 Axons. Neuron 65:230–245.
1202 Denning KS, Reinagel P (2005) Visual control of burst priming in the anesthetized lateral
1203 geniculate nucleus. J Neurosci 25:3531–3538.
1204 Fogerson PM, Huguenard JR (2016) Tapping the Brakes: Cellular and Synaptic Mechanisms that
1205 Regulate Thalamic Oscillations. Neuron 92:687–704.
1206 Gabernet L, Jadhav SP, Feldman DE, Carandini M, Scanziani M (2005) Somatosensory
1207 integration controlled by dynamic thalamocortical feed-forward inhibition. Neuron
1208 48:315–327.
1209 Gentet LJ, Avermann M, Matyas F, Staiger JF, Petersen CCHH (2010) Membrane potential
1210 dynamics of GABAergic neurons in the barrel cortex of behaving mice. Neuron 65:422–435.
1211 Godwin DW, Vaughan JW, Sherman SM (1996) Metabotropic glutamate receptors switch visual
1212 response mode of lateral geniculate nucleus cells from burst to tonic. J Neurophysiol
1213 76:1800–1816.
1214 Greenberg DS, Houweling AR, Kerr JND (2008) Population imaging of ongoing neuronal activity
1215 in the visual cortex of awake rats. Nat Neurosci 11:749–751.
1216 Guo W, Clause AR, Barth-Maron A, Polley DB (2017) A Corticothalamic Circuit for Dynamic
1217 Switching between Feature Detection and Discrimination. Neuron 95:180-194.e5.
1218 Haider B, Häusser M, Carandini M (2013) Inhibition dominates sensory responses in the awake
1219 cortex. Nature 493:97–100.
1220 Halassa MM, Acsády L (2016) Thalamic Inhibition: Diverse Sources, Diverse Scales. Trends
1221 Neurosci 39:680–693.
1222 Halassa MM, Siegle JH, Ritt JT, Ting JT, Feng G, Moore CI (2011) Selective optical drive of
1223 thalamic reticular nucleus generates thalamic bursts and cortical spindles. Nat Neurosci
1224 14:1118–1120.
1225 Heiss JE, Katz Y, Ganmor E, Lampl I (2008) Shift in the Balance between Excitation and Inhibition
1226 during Sensory Adaptation of S1 Neurons. J Neurosci 28:13320–13330.
1227 Hirata A, Castro-Alamancos MA (2010) Neocortex network activation and deactivation states
1228 controlled by the Thalamus. J Neurophysiol 103:1147–1157.
1229 Huguenard JR, McCormick D a. (2007) Thalamic synchrony and dynamic regulation of global
1230 forebrain oscillations. Trends Neurosci 30:350–356.
1231 Jadhav SP, Wolfe J, Feldman DE (2009) Sparse temporal coding of elementary tactile features
1232 during active whisker sensation. Nat Neurosci 12:792–800.
1233 Jin L, Han Z, Platisa J, Wooltorton JRA, Cohen LB, Pieribone VA (2012) Single Action Potentials
1234 and Subthreshold Electrical Events Imaged in Neurons with a Fluorescent Protein Voltage
1235 Probe. Neuron 75:779–785.
1236 Khatri V, Hartings JA, Simons DJ (2004) Adaptation in thalamic barreloid and cortical barrel
1237 neurons to periodic whisker deflections varying in frequency and velocity. J Neurophysiol
1238 92:3244–3254.
1239 Kim HR, Hong SZ, Fiorillo CD (2015) T-type calcium channels cause bursts of spikes in motor but
1240 not sensory thalamic neurons during mimicry of natural patterns of synaptic input. Front
1241 Cell Neurosci 9:428.
1242 Kimura F, Itami C, Ikezoe K, Tamura H, Fujita I, Yanagawa Y, Obata K, Ohshima M (2010a) Fast

activation of feedforward inhibitory neurons from thalamic input and its relevance to the regulation of spike sequences in the barrel cortex. J Physiol 588:2769–2787.

Kimura F, Itami C, Ikezoe K, Tamura H, Fujita I, Yanagawa Y, Obata K, Ohshima M (2010b) Fast activation of feedforward inhibitory neurons from thalamic input and its relevance to the regulation of spike sequences in the barrel cortex. J Physiol 588:2769–2787.

Kirchgessner MA, Franklin AD, Callaway EM (2020) Context-dependent and dynamic functional influence of corticothalamic pathways to first- and higher-order visual thalamus. Proc Natl Acad Sci 117:13066–13077.

Lesica N a, Stanley GB (2004) Encoding of natural scene movies by tonic and burst spikes in the lateral geniculate nucleus. J Neurosci 24:10731–10740.

Lesica N a, Weng C, Jin J, Yeh C-I, Alonso J-M, Stanley GB (2006) Dynamic encoding of natural luminance sequences by LGN bursts. PLoS Biol 4:e209.

Lewis LD, Voigts J, Flores FJ, Ian Schmitt L, Wilson MA, Halassa MM, Brown EN (2015) Thalamic reticular nucleus induces fast and local modulation of arousal state. Elife 4:1–23.

Li L, Ebner FF (2016) Cortex dynamically modulates responses of thalamic relay neurons through prolonged circuit-level disinhibition in rat thalamus in vivo. J Neurophysiol 116:2368–2382.

Litwin-Kumar A, Doiron B (2012) Slow dynamics and high variability in balanced cortical networks with clustered connections. Nat Neurosci 15:1498–1505.

Lustig BR, Friedman RM, Winberry JE, Ebner FF, Roe AW (2013) Voltage-sensitive dye imaging reveals shifting spatiotemporal spread of whisker-induced activity in rat barrel cortex. J Neurophysiol 109:2382–2392.

Ma Y, Shaik MA, Kim SH, Kozberg MG, Thibodeaux DN, Zhao HT, Yu H, Hillman EMC (2016) Wide-field optical mapping of neural activity and brain haemodynamics: considerations and novel approaches. Philos Trans R Soc B Biol Sci 371:20150360.

Massaux A, Dutrieux G, Cotillon-Williams N, Manunta Y, Edeline J-M (2004) Auditory Thalamus Bursts in Anesthetized and Non-Anesthetized States: Contribution to Functional Properties. J Neurophysiol 91:2117–2134.

McCormick DA, Connors BW, Lighthall JW, Prince DA (1985) Comparative electrophysiology of pyramidal and sparsely spiny stellate neurons of the neocortex. J Neurophysiol 54:782–806.

McCormick DA, von Krosigk M (1992) Corticothalamic activation modulates thalamic firing through glutamate “metabotropic” receptors. Proc Natl Acad Sci 89:2774–2778.

Mease RA, Krieger P, Groh A (2014) Cortical control of adaptation and sensory relay mode in the thalamus. Proc Natl Acad Sci 111:6798–6803.

Millard DC, Whitmire CJ, Gollnick CA, Rozell CJ, Stanley GB (2015) Electrical and Optical Activation of Mesoscale Neural Circuits with Implications for Coding. J Neurosci 35:15702–15715.

Murray Sherman S (2001) Tonic and burst firing: Dual modes of thalamocortical relay. Trends Neurosci 24:122–126.

Musall S et al. (2014) Tactile frequency discrimination is enhanced by circumventing neocortical adaptation. Nat Neurosci 17:1567–1573.

Niell CM, Stryker MP (2010) Modulation of visual responses by behavioral state in mouse visual cortex. Neuron 65:472–479.

1287 Niell CM, Stryker MP (2011) Modulation of visual responses by behavioral state in mouse visual
1288 cortex. Neuron 65:472–479.
1289 Olsen SR, Bortone DS, Adesnik H, Scanziani M (2012) Gain control by layer six in cortical circuits
1290 of vision. Nature 483:47–52.
1291 Owen SF, Liu MH, Kreitzer AC (2019) Thermal constraints on in vivo optogenetic manipulations.
1292 Nat Neurosci 22:1061–1065.
1293 Petersen CCH, Grinvald A, Sakmann B (2003) Spatiotemporal dynamics of sensory responses in
1294 layer 2/3 of rat barrel cortex measured in vivo by voltage-sensitive dye imaging combined
1295 with whole-cell voltage recordings and neuron reconstructions. J Neurosci 23:1298–1309.
1296 Pinto DJ, Brumberg JC, Simons DJ (2000) Circuit dynamics and coding strategies in rodent
1297 somatosensory cortex. J Neurophysiol 83:1158–1166.
1298 Poulet JF a, Fernandez LMJ, Crochet S, Petersen CCH (2012a) Thalamic control of cortical states.
1299 Nat Neurosci 15:370–372.
1300 Poulet JFA, Fernandez LMJ, Crochet S, Petersen CCH (2012b) Thalamic control of cortical states.
1301 Nat Neurosci 15:370–372.
1302 Raimondo J V., Kay L, Ellender TJ, Akerman CJ (2012a) Optogenetic silencing strategies differ in
1303 their effects on inhibitory synaptic transmission. Nat Neurosci.
1304 Raimondo J V., Kay L, Ellender TJ, Akerman CJ (2012b) Optogenetic silencing strategies differ in
1305 their effects on inhibitory synaptic transmission. Nat Neurosci 15:1102–1104.
1306 Reinhold K, Lien AD, Scanziani M (2015) Distinct recurrent versus afferent dynamics in cortical
1307 visual processing. Nat Neurosci 18:1789–1797.
1308 Rodenkirch C, Liu Y, Schriver BJ, Wang Q (2019) Locus coeruleus activation enhances thalamic
1309 feature selectivity via norepinephrine regulation of intrathalamic circuit dynamics. Nat
1310 Neurosci 22:120–133.
1311 Sermet BS, Truschow P, Feyerabend M, Mayrhofer JM, Oram TB, Yizhar O, Staiger JF, Petersen
1312 CCH (2019) Pathway-, layer- and cell-type-specific thalamic input to mouse barrel cortex.
1313 Elife 8:1–28.
1314 Sherman SM (2001) A wake-up call from the thalamus. Nat Neurosci 4:344–346.
1315 Sherman SM (2005) Thalamic relays and cortical functioning. In: Progress in Brain Research, pp
1316 107–126.
1317 Sherman SM, Guillery RW (2002) The role of the thalamus in the flow of information to the
1318 cortex Adams P, Guillery RW, Sherman SM, Sillito AM, eds. Philos Trans R Soc London Ser B
1319 Biol Sci 357:1695–1708.
1320 Smith GD, Cox CL, Sherman SM, Rinzel J (2000) Fourier analysis of sinusoidally driven
1321 thalamocortical relay neurons and a minimal integrate-and-fire-or-burst model. J
1322 Neurophysiol 83:588–610.
1323 Speed A, Del Rosario J, Burgess CP, Haider B (2019) Cortical State Fluctuations across Layers of
1324 V1 during Visual Spatial Perception. Cell Rep 26:2868-2874.e3.
1325 Stanley GB, Jin J, Wang Y, Desbordes G, Wang Q, Black MJ, Alonso J-MJ-M (2012) Visual
1326 orientation and directional selectivity through thalamic synchrony. J Neurosci 32:9073–
1327 9088.
1328 Stoelzel CR, Bereshpolova Y, Swadlow H a (2009) Stability of Thalamocortical Synaptic
1329 Transmission across Awake Brain States. J Neurosci 29:6851–6859.
1330 Stujenske JM, Spellman T, Gordon JA (2015) Modeling the Spatiotemporal Dynamics of Light

1331 and Heat Propagation for In Vivo Optogenetics. Cell Rep 12:525–534.
1332 Suzuki M, Larkum ME (2020) General Anesthesia Decouples Cortical Pyramidal Neurons. Cell
1333 180:666-676.e13.
1334 Suzuki S, Rogawski M a (1989) T-type calcium channels mediate the transition between tonic
1335 and phasic firing in thalamic neurons. Proc Natl Acad Sci U S A 86:7228–7232.
1336 Swadlow H a, Gusev a G (2001) The impact of "bursting" thalamic impulses at a neocortical
1337 synapse. Nat Neurosci 4:402–408.
1338 Swadlow HA. (2002) Thalamocortical control of feed–forward inhibition in awake
1339 somatosensory 'barrel' cortex Adams P, Guillery RW, Sherman SM, Sillito AM, eds. Philos
1340 Trans R Soc London Ser B Biol Sci 357:1717–1727.
1341 Swadlow HA, Bezdudnaya T, Gusev AG (2005) Spike timing and synaptic dynamics at the awake
1342 thalamocortical synapse. Prog Brain Res 149:91–105.
1343 Taub AH, Katz Y, Lampl I (2013) Cortical Balance of Excitation and Inhibition Is Regulated by the
1344 Rate of Synaptic Activity. J Neurosci 33:14359–14368.
1345 Urbain N, Salin PA, Libourel PA, Comte JC, Gentet LJ, Petersen CCHH (2015) Whisking-Related
1346 Changes in Neuronal Firing and Membrane Potential Dynamics in the Somatosensory
1347 Thalamus of Awake Mice. Cell Rep 13:647–656.
1348 Varela C (2014) Thalamic neuromodulation and its implications for executive networks. Front
1349 Neural Circuits 8:1–22.
1350 Vizuete JA, Pillay S, Diba K, Ropella KM, Hudetz AG (2012) Monosynaptic functional connectivity
1351 in cerebral cortex during wakefulness and under graded levels of anesthesia. Front Integr
1352 Neurosci 6:1–11.
1353 Wang Q, Webber RM, Stanley GB (2010) Thalamic synchrony and the adaptive gating of
1354 information flow to cortex. Nat Neurosci 13:1534–1541.
1355 Whitmire, CJ, Liew YJ, Stanley GB. Thalamic state influences timing precision in the
1356 thalamocortical circuit, J. Neurophysiol., 125(5):1833-1850, 2021.
1357 Whitmire CJ, Waiblinger C, Schwarz C, Stanley GB (2016) Information Coding through Adaptive
1358 Gating of Synchronized Thalamic Bursting. Cell Rep 14:795–807.
1359 Wright NC, Borden PY, Liew YJ, Bolus MF, Stoy WM, Forest CR, Stanley GB (2021) Rapid Cortical
1360 Adaptation and the Role of Thalamic Synchrony During Wakefulness. J Neurosci:JN-RM-
1361 3018-20.
1362 Wright NC, Hoseini MS, Wessel R (2017a) Adaptation modulates correlated subthreshold
1363 response variability in visual cortex. J Neurophysiol 118:1257–1269.
1364 Wright NC, Hoseini MS, Yasar TB, Wessel R (2017b) Coupling of synaptic inputs to local cortical
1365 activity differs among neurons and adapts after stimulus onset. J Neurophysiol 118:3345–
1366 3359.
1367 Yang H, Kwon SE, Severson KS, O'Connor DH (2016) Origins of choice-related activity in mouse
1368 somatosensory cortex. Nat Neurosci 19:127–134.
1369 Yu J, Gutnisky DA, Hires SA, Svoboda K (2016) Layer 4 fast-spiking interneurons filter
1370 thalamocortical signals during active somatosensation. Nat Neurosci 19:1–14.
1371 Yu J, Hu H, Agmon A, Svoboda K (2019) Recruitment of GABAergic Interneurons in the Barrel
1372 Cortex during Active Tactile Behavior. Neuron 104:412-427.e4.
1373 Zhang C, Yang S, Flossmann T, Gao S, Witte OW, Nagel G, Holthoff K, Kirmse K. Optimized
1374 photo-stimulation of halorhodopsin for long-term neuronal inhibition. BMC Biol. 2019 Nov

27;17(1):95. doi: 10.1186/s12915-019-0717-6.

FIGURE CAPTIONS

Figure 1. Thalamic hyperpolarization amplifies direct feedforward input from thalamus in the anesthetized mouse. A. Pathway of the mouse vibrissa system from the facial vibrissae in the periphery, to brainstem, to thalamus, to S1. **B.** Experimental setup. Mice were injected with the viral vector eNphR3.0 (AAV5-CamIIKianse-eNphR3.0-mCherry) targeting the ventral posterior-medial (VPm) region of the thalamus and the viral vector ArcLight (AAV1-hysn1- ArcLightD- SV40) in the vibrissa region of the primary somatosensory cortex (S1). For optogenetic hyperpolarization, thalamic units were presented with constant illumination (LED, 590 nm, approx. 17 mW/mm^2) from a 200µm optic fiber, with LED illumination starting at 0.5s preceding stimulus (t= -0.5s) and ending 0.5s after stimulus (t=0.5), while recording simultaneously with a single tungsten electrode. Note that unlike for the awake recordings, light presentation was not ramped. For cortical GEVI imaging, the entire cortical area was illuminated through the thinned skull at 465 nm with an LED and imaged with a CCD imaging setup (see Methods). **C.** Thalamic bursts were identified as two or more spikes with inter-spike interval (ISIs) less than 4ms, preceded by silence for 100ms or more. Thalamic spikes that were part of an identified burst were classified as putative burst spikes (red), and all else were classified as tonic spikes (black). **D.** Peri-stimulus time histogram (PSTH) for thalamic spiking in response to a single, punctate whisker stimulus (t=0) for the Control (no light, top panel) and thalamic hyperpolarized (LED, bottom panel) conditions, 29 units. Instantaneous firing rates (bin size 2 ms) shown for all spikes (black) and putative burst spikes (red). **E. Left** Mean sensory-evoked thalamic firing rate (n=29 thalamic units) over the 0 – 30 ms time window increased from the Control (no light) to the LED conditions, for all spikes (black, p= 0.0046, paired Wilcoxon signed-rank) and burst spikes (red, p= 4.5e-4, paired Wilcoxon signed-rank). Error bars represent mean +/- SEM. **Right**. Mean sensory-evoked Cortical multiunit (MU) firing rate from 102 trials (across 2 recordings, 1 mouse, 5ms bin size). **F.** Example session of GEVI imaging following the delivery of a punctate whisker stimulus at time t=0, for the Control (no light, top row) and LED (bottom row) conditions. Images are averaged across 51 trials. Black bar represents 1mm. **G. Left** - Mean normalized peak GEVI sensory-evoked response was larger for the LED as compared to the Control condition (n= 9 mice, 13 recording sessions). For this plot, animals and sessions were each normalized to their control levels, and the LED condition is reported relative to the control. **Left Inset** - raw relative peak evoked %dF/Fo, p=0.017, paired Wilcoxon signed-rank, n=13 recordings across 9 mice. **Right** - Time series of the normalized sensory-evoked GEVI signal, generated from the integrated fluorescence within the 0.2 x 0.2mm ROI in the Control (gray) and LED (orange) conditions. Error bars represent mean +/- SEM.

Figure 2. Thalamic baseline firing rate is invariant to optogenetic hyperpolarization via a tonic/burst switch. A. Experimental setup. Mice were injected with the viral vector eNphR3.0 (AAV5-CamIIKianse-eNphR3.0-mCherry) targeting the ventral posterior-medial (VPm) region of the thalamus. On each trial, thalamic units were presented with light for 1.5 s (590 nm, LED approx. 17mW/mm^2 ramp, Double LED approx. 35mW/mm^2 ramp – see Methods) from a 200µm optic fiber and recorded simultaneously with a single tungsten electrode. **B.** Example

extracellular single trial rasters depicting effects of thalamic hyperpolarization on spiking in VPm thalamus. Black indicates tonic spikes; red indicates burst spikes. Recorded spike waveform shown at top. **C. Top -** Aggregate single-unit (SU, n=5 units) PSTH for all spikes (black) and burst spikes (red). Apparent is an initial decrease in overall firing rate following presentation of light, followed by a return to the pre-hyperpolarization level. **Bottom -** Aggregate multi-unit (MU) activity (n=9 recordings). Bands represent are mean +/- SEM. **D. Left** - Mean multi-unit thalamic firing rate over the 250-750ms time window from the Control (no light) to the LED condition, for all MU spikes (black, Control vs LED p=0.098, Control vs Double LED p=0.65, paired Wilcoxon signrank test, n=9 recordings). **Middle -** Mean single-unit thalamic firing rate over the 250-750ms time window from the Control (no light, n=8 units) to the LED condition (n=5 units), for all spikes (black, Control vs LED p=0.55, Control vs Double LED p=0.37, unpaired t-test) and burst spikes (red, Control vs LED p=0.014, Control vs Double LED p=0.032, unpaired t-test). **Right -** Increase in burst ratio from the Control to LED condition, where burst ratio is defined as the number of burst spikes divided by the total number of spikes (Control vs LED p=0.0016, Control vs Double LED p=0.0016, unpaired Wilcoxon rank sum test). **E. Left -** Example bursts for the Control and LED conditions. **Right -** Increase in the mean number of spikes per burst from the Control to the LED condition (Control vs LED p=0.048, Control vs Double LED p=0.016, unpaired Wilcoxon rank sum test, n=5, only considering cells with bursts). Error bars represent mean +/- SEM. **F.** Simulated spontaneous activity from Integrate-and-fire-or-burst (IFB) model with hyperpolarizing input at time t=0, showing all spikes (black) and burst spikes (red). See Methods and Supplemental Figure S3.

Figure 3. Cortical S1 baseline firing rate is invariant to optogenetic hyperpolarization of thalamus after transient increase. A. Experimental setup. Mice were injected with the viral vector eNphR3.0 (AAV5-CamIIKianse-eNphR3.0-mCherry) targeting the ventral posterior-medial (VPm) region of the thalamus. Thalamic units were continuously presented with light (590 nm, LED approx. 17mW/mm^2 ramp, Double LED approx. 35mW/mm^2 ramp) from a 200µm optic fiber, while cortical single-units were recorded simultaneously with a laminar multi-electrode within an identified cortical column (barrel) – see Methods. **B. Top -** Example extracellular rasters of cortical activity, depicting effects of thalamic hyperpolarization on cortical spiking, across trials and simultaneously recorded units (10 trials each from 15 units). **Bottom -** Aggregate PSTH across all recorded trials and cortical single-units (n=118). Bands represent mean +/- SEM. Highlighted are the transient and steady-state portions of the cortical response to the light. **C.** Mean cortical firing rate in the Control and LED conditions, showing an increase in the transient (open symbol, 300-350ms, Control vs LED p=5.4e-14, Control vs Double LED p=1.4e-15, Wilcoxon signed-rank test) and a return to near steady-state (closed symbol, 700-750ms, Control vs LED p=0.2, Control vs Double LED p=0.013, Wilcoxon signed-rank test) portions of the response. Error bars represent mean +/- SEM.

Figure 4. Thalamic hyperpolarization amplifies the thalamic but not cortical sensory-evoked response in the awake mouse. A. Experimental setup. Mice were injected with the viral vector eNphR3.0 (AAV5-CamIIKianse-eNphR3.0-mCherry) targeting the ventral posterior-medial (VPm) region of the thalamus and the viral vector ArcLight (AAV1-hysn1- ArcLightD- SV40) in the vibrissa region of the primary somatosensory cortex (S1). For optogenetic hyperpolarization, on each trial

thalamic units were presented with light for 1.5 s (590 nm, LED approx. 17mW/mm^2 ramp, Double LED approx. 35mW/mm^2 ramp – see Methods) from a 200µm optic fiber, with LED illumination beginning at 0.75s preceding stimulus delivery, and continuing for 0.75s after stimulus delivery, while recording simultaneously with a single tungsten electrode. For cortical GEVI imaging, the entire cortical area was illuminated through the thinned skull at 465 nm with an LED and imaged with a CCD imaging setup (see Methods). **B.** Grand Multiunit PSTH for thalamic spiking in response to a single, punctate whisker stimulus (t=0) for the Control (no light, top panel, n=9 recordings) and LED (bottom panel, n=9 recordings) conditions. Instantaneous firing rates (bin size 2 ms) shown for all spikes (black). **C.** Mean sensory-evoked thalamic response over 0-30ms time window for multi-unit recordings (Control vs LED p=0.0039, Control vs Double LED p=0.0039, unpaired Wilcoxon rank sum, n=9). Error bars represent mean +/- SEM. **D.** Grand single unit PSTH for thalamic spiking in response to a single, punctate whisker stimulus (t=0) for the Control (no light, top panel, n=8 units) and LED (bottom panel, n=5 units) conditions. Instantaneous firing rates (bin size 2 ms) shown for all spikes (black) and putative burst spikes (red). **E.** Mean single-unit sensory-evoked thalamic burst ratio over the 0–30 ms time window (Control vs LED p=0.011, Control vs Double LED p=0.019, unpaired Wilcoxon rank sum Control n=8 units, LED conditions n=5 units). **F.** Example session of GEVI imaging following the delivery of a punctate whisker stimulus at time t=0, for the Control (no light, top row) and LED (bottom row) conditions. Images are averaged across 51 trials. **G. Left** - Peak GEVI sensory-evoked response (between 0-110ms post stimulus) slightly decreased from the Control to the LED condition (Control vs LED p=0.020, Control vs Double LED p=0.0039, paired Wilcoxon signrank, n=9 recordings from 2 mice). **Right -** Mean normalized peak GEVI sensory-evoked response for the Control and LED conditions (n=9 recordings). Before combining, animals and sessions were each normalized to their Control levels, and the LED condition is reported relative to the Control. **H.** In separate experiments, we hyperpolarized the thalamus while simultaneously recording the S1 Cortical response using a multichannel electrode. **I.** Cortical Grand PSTH evoked sensory response (t=0) across all recorded single units (n=118 units, 5ms bins) for Control (black) and LED (orange) conditions. **J. Left** Average absolute evoked cortical response remained approximately invariant during LED on conditions across all cortical recorded units (n=118). Evoked sensory response period defined as between 5-100ms post stimulus. **Right.** Relative evoked cortical response decreased with increasing LED intensities (Control vs LED p=0.20, Control vs Double LED p=0.034, paired Wilcoxon signrank, n=118 units). Relative evoked response defined as the absolute response minus the preceding baseline activity -50-0ms pre-stimulus. Error bars represent mean +/- SEM.

Figure 5. Thalamic hyperpolarization sharpens the spatial and temporal cortical sensory evoked response revealed through GEVI imaging. A. GEVI imaging frames at peak response for the control (top) and LED (bottom) conditions for an example session. **B.** Cartoon illustration of the coupling between amplitude and spatial area in cortical imaging. **Top -** A reduction in evoked fluorescence amplitude can be qualitatively perceived as a reduction in spatial area of activation, due to the "iceberg" effect. **Bottom -** However, the spatial area of activation above a fixed threshold after normalization to the peak reveals the true effects on the area. **C.** Normalized amplitude time series of fluorescence within R0I for Control (black) and thalamic hyperpolarized (orange, LED), n= 9 recordings from 2 mice) conditions. Bands represent mean +/- SEM. **D.**

Summary analyses (Error bars represent mean +/- SEM). Note, for this figure all conditions are normalized to their respective peak responses, as portrayed in B. **Left** - Mean spatial activation area of the normalized sensory-evoked response decreased from the Control to the LED condition (Control vs LED p=0.025, Control vs Double LED p=0.046, paired t-test, n= 9 recordings). **Middle** - The peak-to-baseline (defined in Figure 5C), calculated as the mean time from the peak of the fluorescence to the first return to pre-stimulus baseline (ms), decreased from the Control to the LED condition (Control vs LED p=0.0059, Control vs Double LED p=0.0019, unpaired t-test, n= 8 Control recordings, 9 LED recordings, note one of the Control recordings did not return to baseline). **Right** – The recovery (defined in Figure 5C), calculated as the relative mean fluorescence during the time duration following the peak stimulus-evoked response (120-400ms), decreased from the Control to the LED condition (Control vs LED p=0.016, Control vs Double LED p=0.020, paired t-test, n= 9 recordings). LED approx. 17mW/mm^2 ramp, Double LED approx. 35mW/mm^2 ramp – see Methods. Error bars represent mean +/- SEM.

Figure 6. Thalamic hyperpolarization affects timing but not magnitude of sensory-evoked responses in cortex. A. Cortical single-units were classified as Regular Spiking Units (RSUs, red) or Fast Spiking Units (FSUs, blue) based on the time interval from the peak-to-trough (see Methods). Example RSU and FSU waveforms are shown at the top, where bands represent +/- 1 SD. The distribution of time intervals from peak-to-trough for the spike waveforms is shown at the bottom. **B.** PSTHs of the aggregate putative FSUs (left, n=32) and RSUs (right, n=86) in response to a punctate whisker deflection at time t=0 (bin size 2ms) for the Control (black) and double LED (orange) conditions. **C.** Summary analyses (Error bars represent mean +/- SEM) for RSUs (top row) and FSUs (bottom row). **Left** - Mean baseline (-50 to 0ms) RSU (Control vs LED p=5.3e-4, Control vs Double LED p=0.012, Wilcoxon signed-rank test, n=86) and FSU (Control vs LED p=0.15, Control vs Double LED p=0.30, Wilcoxon signed-rank test, n=32) firing rates for the LED relative to the Control condition. **Middle** - RSU (Control vs LED p=0.067, Control vs Double LED p=0.0082, Wilcoxon signed-rank test, n=86) and FSU (Control vs LED, p=0.30, Control vs Double LED p=0.45, Wilcoxon signed-rank test, n=32) early sensory response (5-50ms) for the LED compared to the Control conditions. **Right** – Late sensory response (60-100ms) for the LED compared to the Control condition for the RSU (Control vs LED p=0.017, Control vs Double LED p=0.014, n=86, Wilcoxon signed-rank test) and FSU (Control vs LED p=2.2e-4, Control vs Double LED p=4.5e-4, n=32, Wilcoxon signed-rank test) populations. LED approx. 17mW/mm^2 ramp, Double LED approx. 35mW/mm^2 ramp – see Methods. Error bars represent mean +/- SEM.

Figure 7. Thalamic hyperpolarization enhances cortical synchrony. A. The spike cross-correlogram (CCG) was calculated as a histogram of spike times of cell 2 relative to a target spike of cell 1, repeated for all spikes of cell 1. The pair-wise synchrony was calculated from the CCG as the area of the CCG between +/- 7.5ms, normalized by the total area of the CCG. **B**. **Top** Example Raster of two simultaneously collected FSU units, Cell 1 (black), Cell 2 (purple) for Control and LED conditions. **Bottom**. Synchronous spiking events only for the same neural pair (red, firing within 7.5ms of each other). **C.** Aggregate cross-correlograms for FSUs (n=99 pairs, see Methods) for the control (black) and LED (orange) conditions. Note that for the LED condition, the light level was 35 mW/mm^2 to better emphasize the change in synchrony with thalamic hyperpolarization. Cross-correlograms have been smoothed via a moving average filter, 2.5ms window. **D.** Mean

levels of synchrony FSU pairs, for the spontaneous/baseline cortical firing as compared to the sensory-evoked response for the Control and LED conditions. Relative to the Control condition, thalamic hyperpolarization (LED, 35mW/mm^2) resulted in an increase in synchrony for the FSU (Control vs LED, p=1.5e-8, Control vs Double LED, p=3.5e-13, Wilcoxon signed-rank test, n=99 pairs) populations. LED approx. 17mW/mm^2 ramp, Double LED approx. 35mW/mm^2 ramp – see Methods. Error bars represent mean +/- SEM.

Figure 8. A thalamocortical network model with TC synaptic adaptation reproduces three key experimental results. A. Thalamocortical model schematic (see Methods). A clustered network of excitatory (red) and inhibitory (blue) neurons received inputs from a model VPm barreloid, as well as random excitatory inputs. Thalamocortical synapses instantly depressed and slowly recovered in response to a VPm spike. **B.** Grand mean PSTHs for VPm tonic and burst spikes (top) and network excitatory and inhibitory neurons (bottom), for the Control (black) and LED (orange) conditions. **Insets:** same, but for 60 – 100 ms post-stimulus window. **C. Left** - Grand mean (+/- SEM) rates for all model VPm (black), excitatory (red) and inhibitory (blue) neurons for the early (0 – 50 ms post-stim, left) response window. VPm control: 28.08 +/- 2.04 Hz; VPm LED: 34.53 +/- 2.67 Hz; 23.0 % increase, p = 2.16 x 10^{-7}, Wilcoxon signed-rank test. Excitatory control: 11.24 +/- 0.3 Hz; excitatory LED: 11.41 +/- 0.32 Hz; 1.53% increase, p = 0.34. Inhibitory control: 143.39 +/- 2.85 Hz; inhibitory LED: 142.73 +/- 2.76 Hz; 0.46% decrease, p = 0.61. **Right** – Same, but for late (60 – 100 ms post-stim, right) response window. VPm control: 7.02 +/- 0.64 Hz; VPm LED: 2.28 +/- 0.29 Hz; 67.6% decrease, p = 1.50 x 10^{-7}. Excitatory control: 3.23 +/- 0.11 Hz; excitatory LED: 1.42 +/- 0.08 Hz; 56.0% decrease, p = 4.94 x 10^{-90}. Inhibitory control: 47.38 +/- 1.71 Hz; inhibitory LED: 17.95 +/- 1.27 Hz; 62.1% decrease, p = 3.86 x 10^{-18}. **D.** Grand cross-correlograms for 147 randomly-selected, valid pairs of network excitatory neurons (see Model Supplement Section 1). **E. Left** - Same as in (D), but for window used to calculate synchrony (+/- 7.5 ms). **Right** - Grand mean pairwise synchrony for excitatory pairs used to generate CCGs in D, left. Exc-exc synchrony control: 0.56 +/- 0.02; exc-exc synchrony LED: 0.66 +/- 0.02; p = 3.03 x 10^{-7}, control vs. LED. **F, G.** Same as in (D, E), but for 200 randomly-selected, valid network inhibitory neurons. Inh-inh synchrony control: 0.53 +/- 0.003; inh-inh synchrony LED: 0.60 +/- 0.003; p = 1.44 x 10^{-34}, control vs. LED. * Indicates 0.01 ≤ p < 0.05, ** indicates 0.001 ≤ p < 0.01, *** indicates p < 0.001, Wilcoxon signed-rank test.

Figure 1

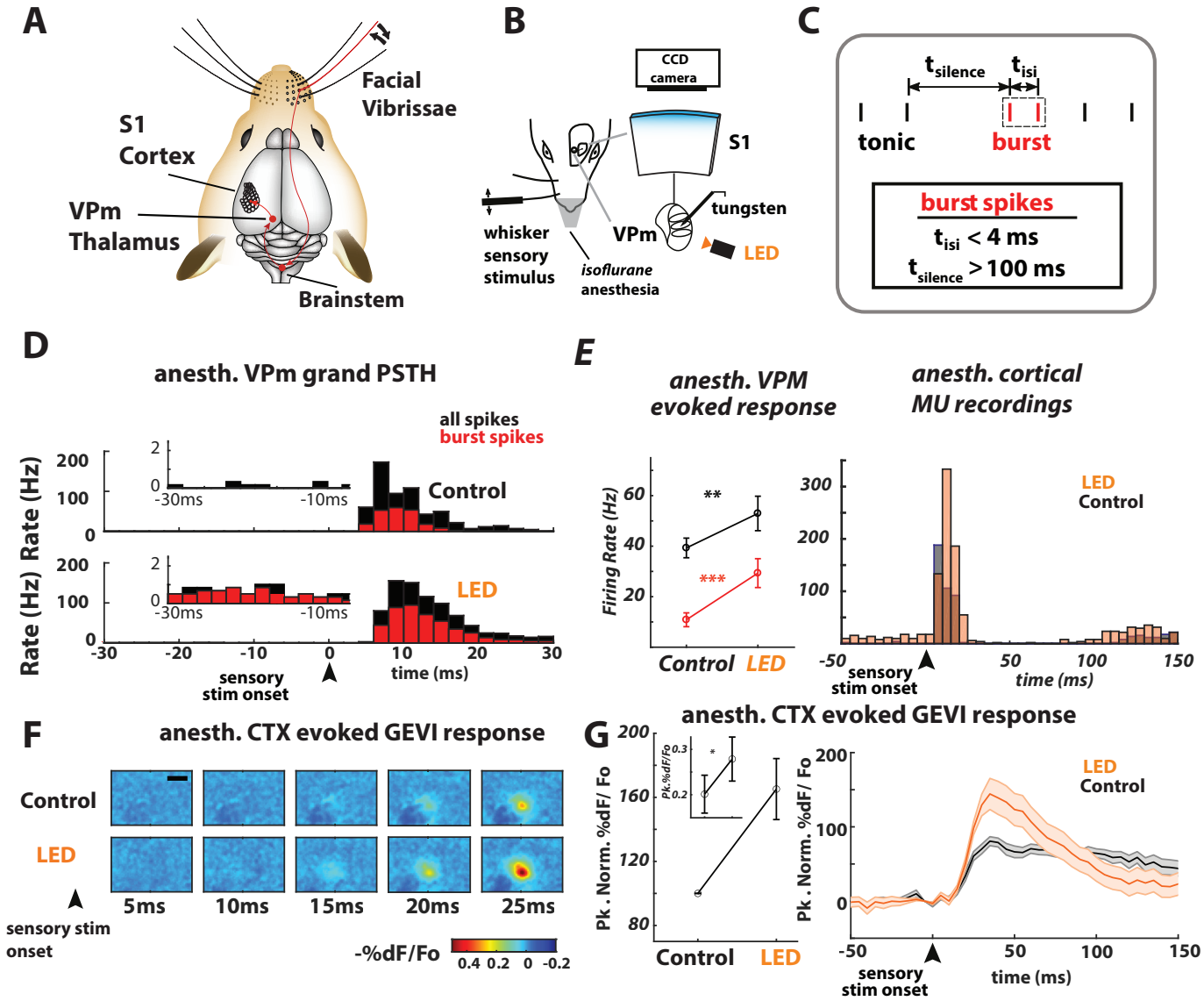
A
Facial Vibrissae
S1 Cortex
VPm Thalamus
Brainstem
B
CCD camera
S1
tungsten
whisker sensory stimulus
VPm
LED
isoflurane anesthesia
C
t silence
t isi
tonic
burst
burst spikes
t isi < 4 ms
t silence > 100 ms
D
anesth. VPm grand PSTH
all spikes
burst spikes
Control
LED
Rate (Hz)
-30ms
-10ms
sensory stim onset
time (ms)
E
anesth. VPM evoked response
anesth. cortical MU recordings
Firing Rate (Hz)
Control
LED
sensory stim onset
time (ms)
F
anesth. CTX evoked GEVI response
Control
LED
5ms
10ms
15ms
20ms
25ms
sensory stim onset
-%dF/Fo
G
anesth. CTX evoked GEVI response
Pk. Norm. %dF/ Fo
Pk.%dF/Fo
Control
LED
sensory stim onset
time (ms)

Figure 2

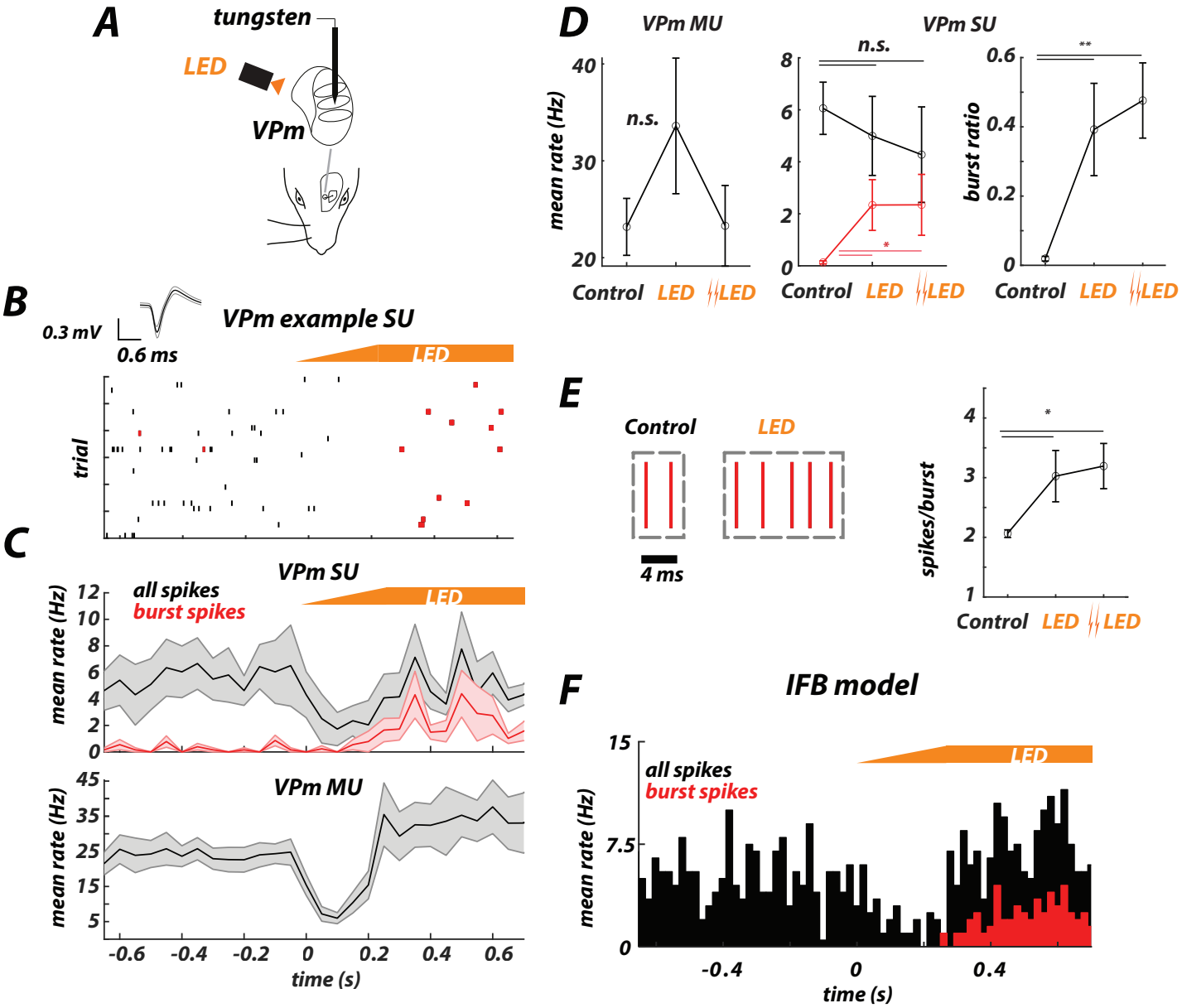
A
tungsten
LED
VPm
B
0.3 mV
0.6 ms
VPm example SU
LED
trial
C
VPm SU
all spikes
burst spikes
LED
mean rate (Hz)
VPm MU
time (s)
D
VPm MU
VPm SU
n.s.
mean rate (Hz)
burst ratio
Control
LED
LED
E
Control
LED
4 ms
spikes/burst
F
IFB model
all spikes
burst spikes
LED
mean rate (Hz)
time (s)

Figure 3

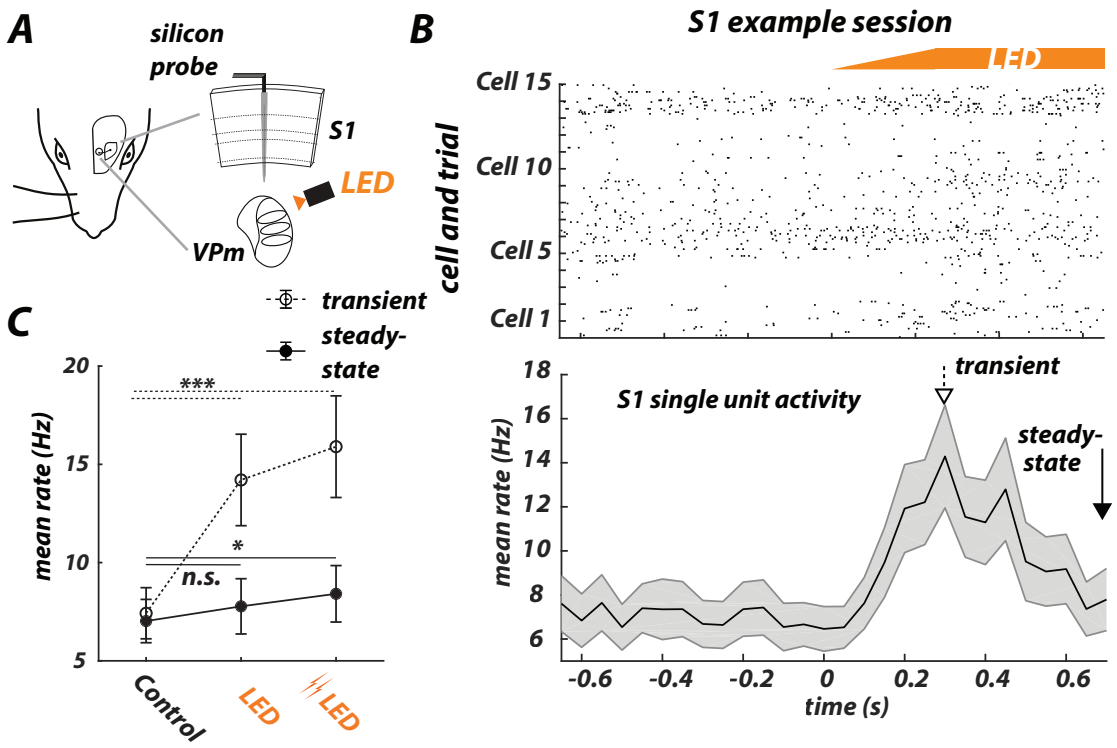
A
silicon
probe
S1
LED
VPm
B
S1 example session
LED
Cell 15
Cell 10
Cell 5
Cell 1
cell and trial
S1 single unit activity
transient
steady-
state
mean rate (Hz)
18
16
14
12
10
8
6
-0.6
-0.4
-0.2
0
0.2
0.4
0.6
time (s)
C
transient
steady-
state
20
15
10
5
***
*
n.s.
Control
LED
LED

Figure 4

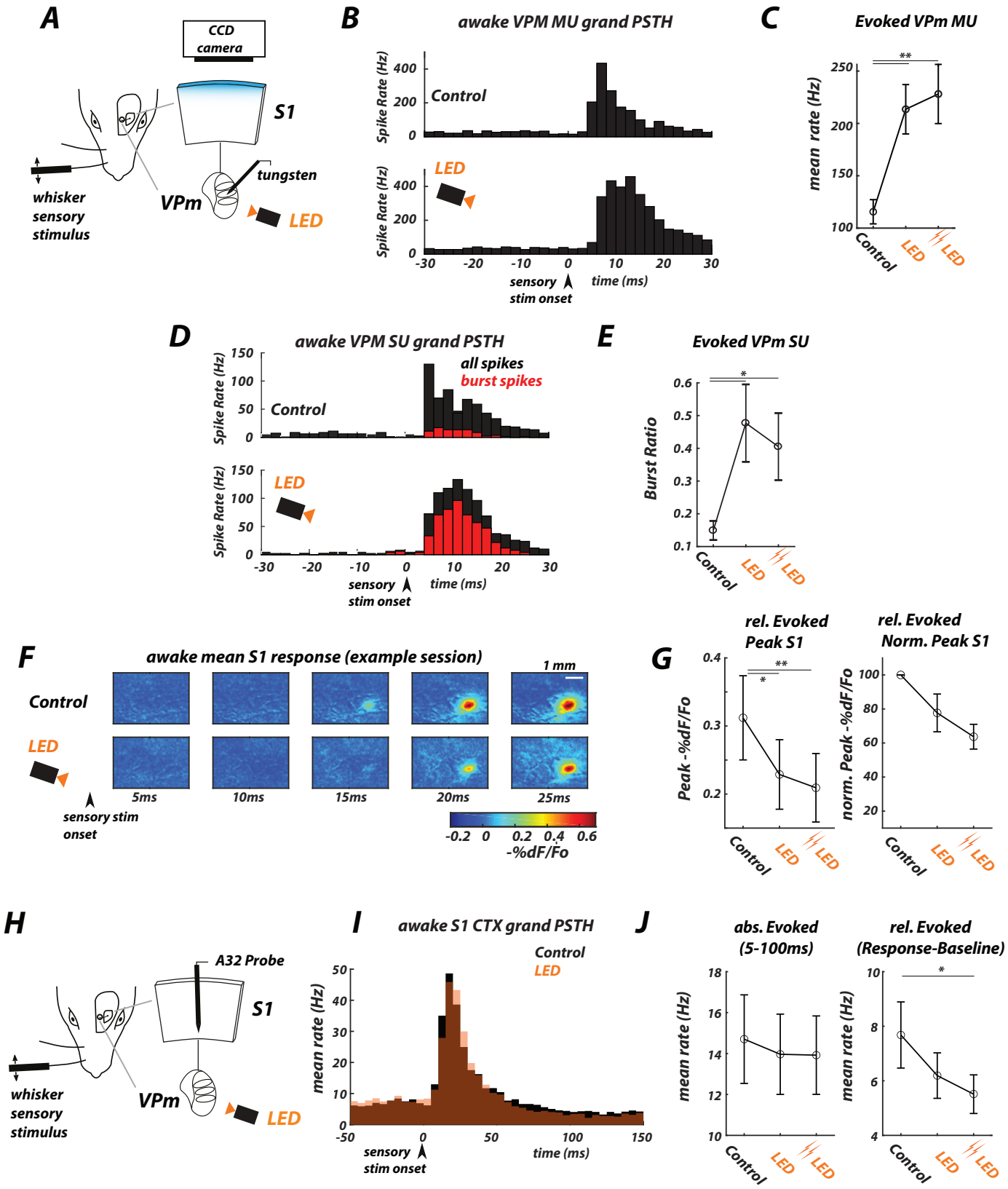
A
CCD camera
S1
tungsten
whisker sensory stimulus
VPm
LED
B
awake VPM MU grand PSTH
Spike Rate (Hz)
Control
LED
sensory stim onset
time (ms)
C
Evoked VPm MU
mean rate (Hz)
Control
LED
D
awake VPM SU grand PSTH
all spikes
burst spikes
E
Evoked VPm SU
Burst Ratio
F
awake mean S1 response (example session)
1 mm
5ms
10ms
15ms
20ms
25ms
-%dF/Fo
G
rel. Evoked Peak S1
rel. Evoked Norm. Peak S1
Peak -%dF/Fo
norm. Peak -%dF/Fo
H
A32 Probe
I
awake S1 CTX grand PSTH
J
abs. Evoked (5-100ms)
rel. Evoked (Response-Baseline)

Figure 5

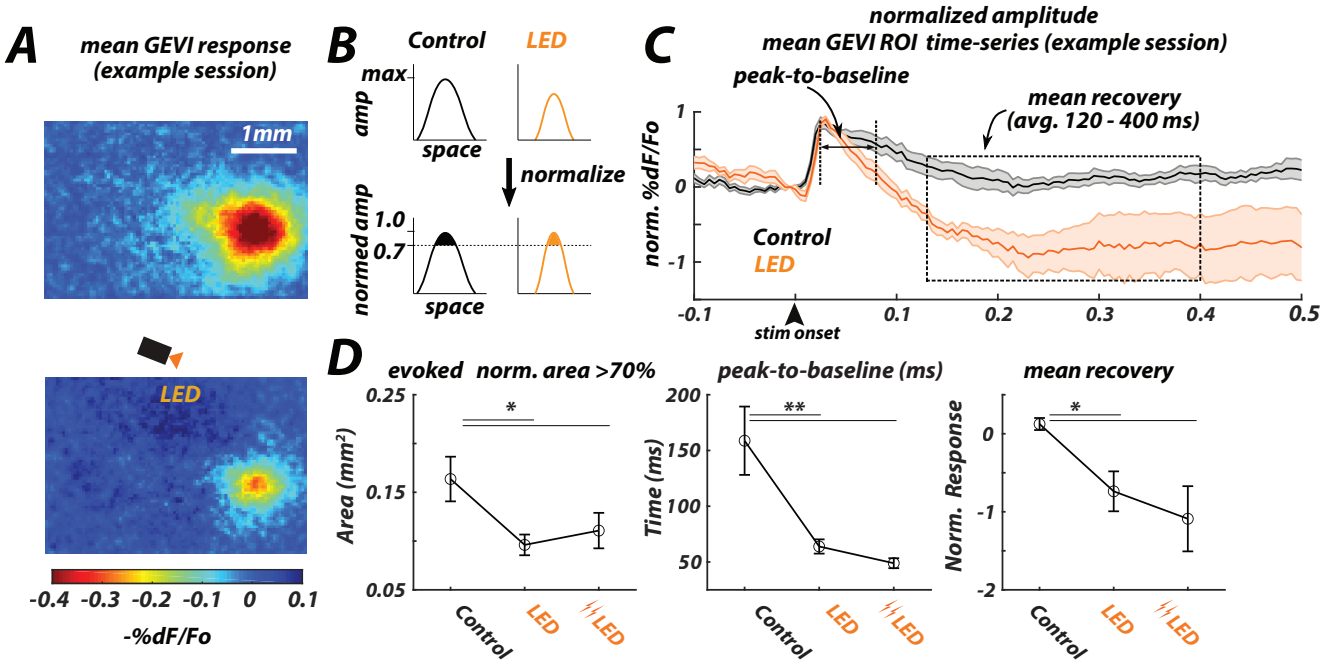
A
mean GEVI response
(example session)
1mm
LED
-0.4 -0.3 -0.2 -0.1 0 0.1
-%dF/Fo
B
Control
LED
max
amp
space
normalize
normed amp
1.0
0.7
space
C
normalized amplitude
mean GEVI ROI time-series (example session)
peak-to-baseline
mean recovery
(avg. 120 - 400 ms)
norm. %dF/Fo
1
0
-1
Control
LED
-0.1
0.1
0.2
0.3
0.4
0.5
stim onset
D
evoked norm. area >70%
Area (mm²)
0.25
0.15
0.05
*
Control
LED
LED
peak-to-baseline (ms)
Time (ms)
200
150
100
50
**
Control
LED
LED
mean recovery
Norm. Response
0
-1
-2
*
Control
LED
LED

Figure 6

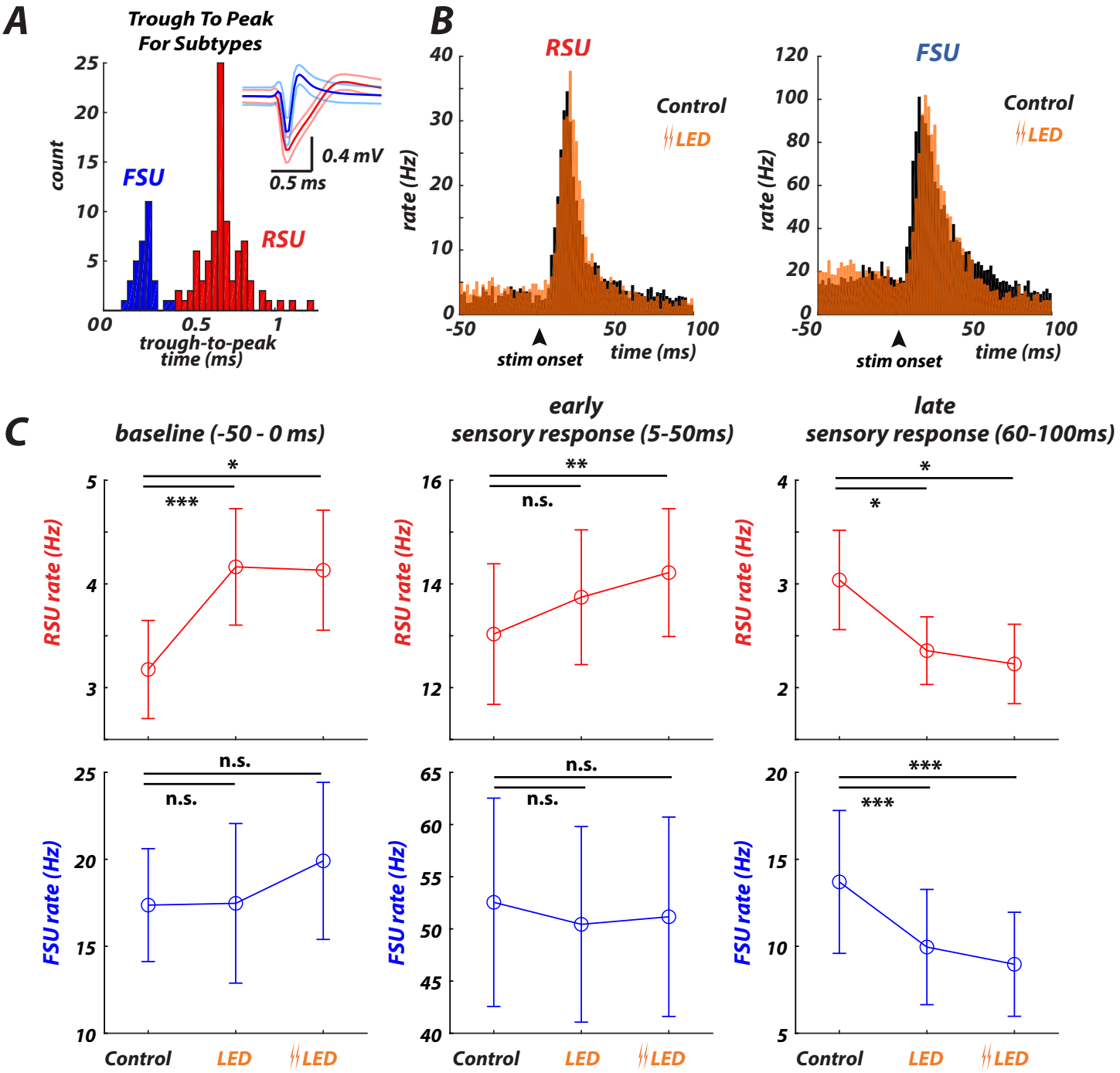
A
Trough To Peak
For Subtypes
count
FSU
RSU
0.4 mV
0.5 ms
trough-to-peak
time (ms)
B
RSU
Control
LED
rate (Hz)
stim onset
time (ms)
FSU
Control
LED
rate (Hz)
stim onset
time (ms)
C
baseline (-50 - 0 ms)
early
sensory response (5-50ms)
late
sensory response (60-100ms)
RSU rate (Hz)
FSU rate (Hz)
n.s.
Control
LED
LED

Figure 7

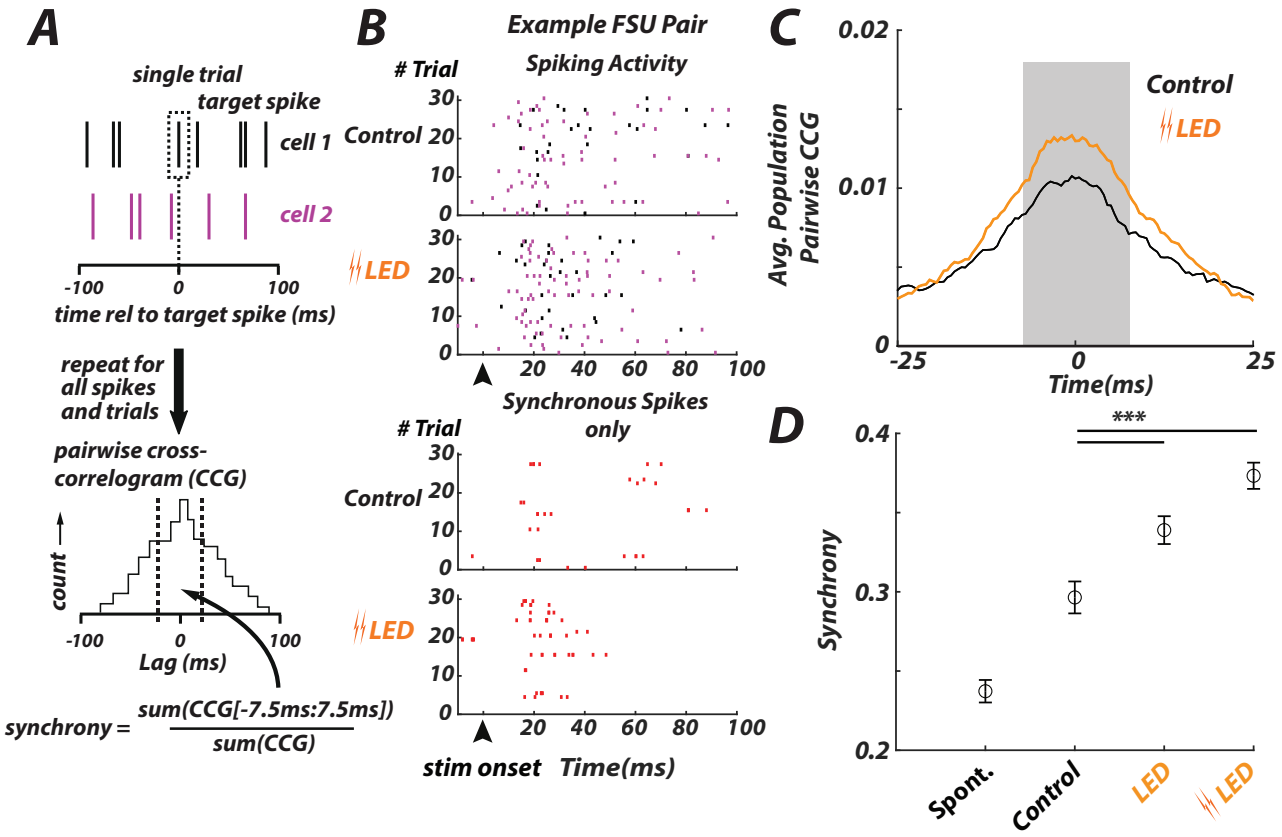
A
single trial
target spike
cell 1
cell 2
-100
0
100
time rel to target spike (ms)
repeat for all spikes and trials
pairwise cross-correlogram (CCG)
count
-100
0
100
Lag (ms)
synchrony = sum(CCG[-7.5ms:7.5ms]) / sum(CCG)
B
Example FSU Pair
Spiking Activity
Trial
Control
LED
30
20
10
0
20
40
60
80
100
Synchronous Spikes only
stim onset
Time(ms)
C
0.02
0.01
0
Avg. Population Pairwise CCG
Control
LED
-25
0
25
Time(ms)
D
***
0.4
0.3
0.2
Synchrony
Spont.
Control
LED
LED

Figure 8

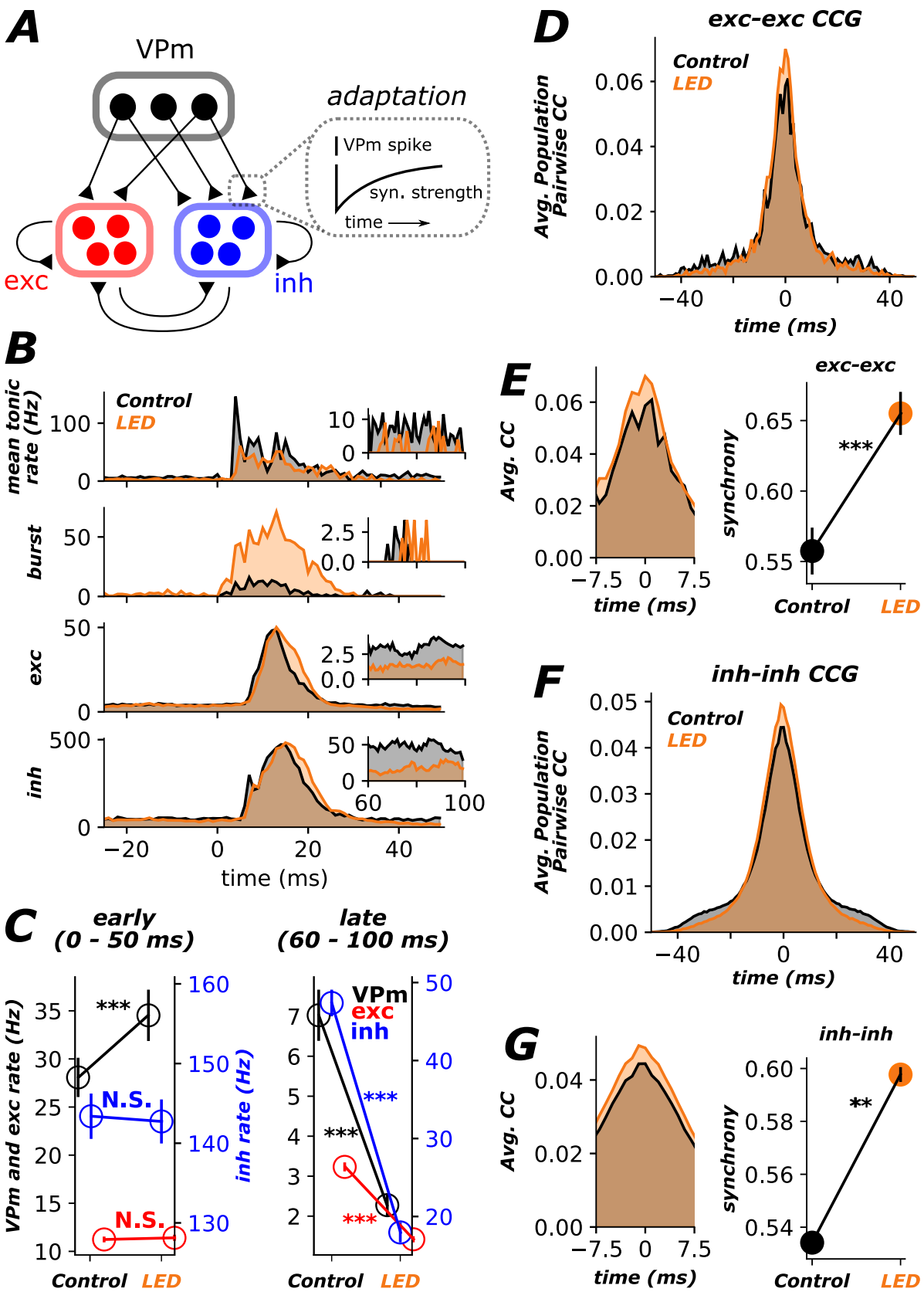
A
VPm
adaptation
VPm spike
syn. strength
time
exc
inh
B
mean tonic rate (Hz)
Control
LED
burst
exc
inh
time (ms)
C
early (0 - 50 ms)
late (60 - 100 ms)
VPm and exc rate (Hz)
inh rate (Hz)
***
N.S.
VPm
exc
inh
Control
LED
D
exc-exc CCG
Avg. Population Pairwise CC
time (ms)
E
exc-exc
Avg. CC
synchrony
F
inh-inh CCG
G
inh-inh
**